Petroleum Science 23 (2026) 692–711

Contents lists available at ScienceDirect

Petroleum Science

journal homepage: www.keaipublishing.com/en/journals/petroleum-science

Original Paper

Adsorption behavior of spherical pores in shale integrated with simplified local density theory

Yu Zhao, Da-Guo Quan, Chao-Lin Wang *, Kun-Peng Zhang

College of Civil Engineering, Guizhou University, Guiyang, 550025, Guizhou, China

ARTICLE INFO

Article history:
Received 31 March 2025
Received in revised form
2 July 2025
Accepted 8 September 2025
Available online 16 September 2025

Eidted by Meng-Jiao Zhou

Keywords:
SLD model
Spherical pore
Adsorption
Density profile
Shale

ABSTRACT

Shale is a strongly heterogeneous anisotropic porous medium with a complex nanopore structure. Therefore, accurately describing the distribution and occurrence of shale gas in the intricate pore structure of shale is difficult. The simplified local density (SLD) theory constitutes an effective and widely accepted approach for characterizing the adsorption mechanism within the intricate pore structures of nanoporous shale. On the basis of SLD theory, this paper proposes for the first time a new adsorption model that considers spherical pores to accurately describe the adsorption behavior within the complex pore structure of shale containing spherical pores. Compared with conventional adsorption theory models and traditional SLD models, not only were the accuracy and applicability of the new model verified, but it was also found that the new model could significantly improve the effective calculation accuracy even with fewer fitting parameters. Furthermore, an analysis of and discussing the adsorption behavior of methane in shale pores with different pore structures (including pore geometries, specific surface areas, diameters and volumes) revealed that the pore structure significantly affects the adsorption behavior of methane. The effects of the number of pore wall solid molecular layers that characterize different fluid-solid interactions and the adjustable parameters for repulsive forces that characterize different fluid-fluid interactions on the methane adsorption isotherms and density distributions were also explored. The results indicate that the newly developed spherical SLD model may provide new insights into the occurrence mode of shale gas in complex shale pores and offer valuable references for reserve assessment and extraction efficiency optimization in shale gas exploration.

1. Introduction

Shale gas, regarded as an unconventional natural gas resource, constitutes an increasingly significant portion of the global energy supply. Numerous countries worldwide have undertaken extensive exploration and development initiatives (Sun et al., 2021; Montgomery et al., 2005; Chalmers and Bustin, 2008; Tang et al., 2020). The methane content in shale gas exceeds 94%, but it contains only small amounts of alkanes and trace carbon dioxide and nitrogen. Its combustion produces fewer pollutants, making it more environmentally friendly than traditional fossil energy sources do (Kalkreuth et al., 2013). In the shale pore structure, natural gas occurs in three distinct forms: adsorbed onto the pore surfaces, free within the pore spaces, and dissolved within the shale matrix (Curtis, 2002; Ross and Bustin, 2008; Bernard et al., 2010). Among these, gas is stored on the surface of both organic matter and inorganic minerals within shale through physical adsorption, potentially accounting for up to 80% of the total pore gas volume (Edwards et al., 2015). This adsorption mechanism has doubled the gas storage capacity in pores and formed a high-density adsorption layer on the surface (Tinni et al., 2017; Brunauer et al., 1940). Therefore, in-depth exploration of the physical adsorption mechanism of shale has an important guiding role in evaluating and developing shale gas reserves.

At present, methods for accurately predicting gas adsorption behavior mainly include laboratory adsorption experiments (Chen et al., 2018; Wang et al., 2024), commonly used theoretical models (Langmuir, 1918; Brunauer et al., 1938; Ono and Kondo, 1960; Dubinin, 1967; Yao et al., 2008), molecular simulations (Yang et al., 2020; Wang et al., 2019) and functional computational

* Corresponding author.
E-mail address: chaolinwang@126.com (C.-L. Wang).
Peer review under the responsibility of China University of Petroleum (Beijing).

https://doi.org/10.1016/j.petsci.2025.09.012

models (Guo et al., 2024; Fitzgerald et al., 2006; Wu et al., 2019). In laboratory settings, the adsorption capacity of samples can be evaluated via two principal methods: the volumetric method and the gravimetric method (Gasparik et al., 2014a, 2014b). Notably, the volumetric method has been predominantly employed to assess gas adsorption, matrix deformation, and permeability in shale and coal substrates (Santos and Akkutlu, 2013; Zeng et al., 2017). This method operates on the principle of indirectly determining the adsorption quantity at each pressure point by measuring changes in gas pressure within the container, thereby generating the sample's adsorption isotherm. Nevertheless, what is typically measured in the laboratory is the excess adsorption isotherm, also referred to as the Gibbs gas adsorption isotherm. Furthermore, owing to the variation in adsorbed phase volume with pressure, the absolute adsorption amount cannot be directly measured in the laboratory (Sudibandriyo et al., 2003). In conclusion, although the amount of methane adsorbed by shale can be obtained through laboratory adsorption experiments, it is still necessary to find a suitable model to further characterize the adsorption mechanism of shale.

A variety of theoretical models are frequently employed in the study of adsorption. Existing theoretical calculation models include the Langmuir, Brunauer-Emmett-Teller (BET), Dubinin-Radushkevich (D-R) or Dubinbin-Astakhov (D-A), Ono-Kondo (O-K) and fractal adsorption (F-A) models. Additionally, there is an empirical formula known as the Freundlich isotherm. Notably, the Langmuir model is predominantly employed to characterize the adsorption behavior of monolayer gas molecules on the surface of adsorbents and is regarded as one of the classical models for describing adsorption isotherms (Swenson and Stadie, 2019). Brunauer et al. (1938) proposed that there was an interaction between molecular layers, so they proposed a BET model to describe multimolecular layer adsorption on the basis of monolayer adsorption. The D-R and D-A models, as proposed by Huber et al. (1978) and Dubinin and Astakhov (1971), indicate that gas molecules do not adsorb onto the pore surface but instead fill the micropores. Ono and Kondo (Pang and Jin, 2019) built the O-K lattice model on the basis of lattice theory, which assumes that gas molecules reach adsorption equilibrium at the lattice position. According to the F-A model, the adsorption behavior of adsorbents with a fractal geometry relationship also has fractal characteristics after adsorption (Pfeifer et al., 1997). Furthermore, the Freundlich model, which serves as an empirical equation, predicts the adsorption isotherm through the relationship between the amount of adsorption and the equilibrium pressure (Appel, 1973). However, the majority of these models are primarily suited for predicting coalbed methane adsorption and exhibit certain limitations in accurately characterizing methane adsorption behavior within shale pores (Pang Y et al., 2020; Zeng et al., 2024). First, most of these models incorporate multiple empirical parameters that require conversion into gas density parameters to adequately represent the Gibbs gas adsorption capacity. Second, these methods generally fail to precisely delineate the regions of adsorbed and bulk phases within the pore structure. Most critically, these theoretical models do not provide a precise explanation of how pore structure influences adsorption behavior. While molecular simulation (MS) and density functional theory (DFT) can accurately describe adsorption isotherms and phase behavior in pores (Barrera et al., 2013; Gor et al., 2012), their computational processes are complex and time-consuming (Rangarajan et al., 1995).

The simplified local density (SLD) theory effectively solves the above problems. It has a high calculation speed and high precision. It is also able to predict adsorption isotherms and density distributions in shale nanopores by combining the interaction potential function used to characterize shale pore structure with the fluid equation of state (EOS), which characterizes fluid-fluid interactions. SLD theory is a method for calculating the adsorbed phase density proposed by Rangarajan et al. (1995) on the basis of the mean field hypothesis. Initially, this theory was only applicable to the calculation of the adsorbed phase density on a semi-infinite surface. To address the actual situation, Chen et al. (1997) further proposed a calculation method for the adsorption capacity of slit pores of different widths on the basis of semi-infinite planes. Fitzgerald et al. (2003) demonstrated that modifying the repulsive force parameters in the equation of state for gases significantly influences the fitting accuracy of the slit SLD model. Hasanzadeh et al. (2010) employed the slit SLD model to investigate the adsorption behavior of binary gas mixtures within slit pores. Zeng et al. (2017b) developed a slit SLD model for competitive adsorption of water and methane, thereby quantifying their respective adsorption behaviors in porous media. Since the above studies were all aimed at slit pores, Chen et al. (2018) expanded the pore shape and established the SLD model of cylindrical pores. Pang et al. (2020) further characterized adsorption isotherms and density profiles in cylindrical pores. By integrating cylindrical SLD theory with nuclear magnetic resonance (NMR) technology, Wang et al. (2022) were able to determine the pore size distribution of a sample and accurately predict the quantity of gas adsorbed within the pores. Zeng et al. (2024) examined the interaction between gas molecules and solid molecules on the pore wall via the cylindrical SLD model under the (3/8) σ_{ff} hypothesis and compared the density distribution characteristics under various modified parameters Λ_b. However, through extensive studies of field emission scanning electron microscopy (FESEM) images (Afsharpoor and Javadpour, 2016; Sun et al., 2020; Yin et al., 2022; Gao et al., 2021; Cao et al., 2019; Zhao et al., 2022; Wang et al., 2021), it was found that in addition to slit and cylindrical nanopores, there are also abundant spherical nanopores within the organic matter (OM) of shale, as shown in Fig. 1.

The numerous nanoscale pores within the shale OM provide effective storage space for shale gas. However, the shape and size of nanoscale pores significantly affect gas adsorption and desorption as well as gas transport and migration. Therefore, to investigate the influence of varying pore structures on the adsorption mechanism of shale, this study establishes a novel adsorption model based on the SLD theory. Unlike the conventional SLD model, which accounts for slit and cylindrical pores, this study considers spherical pores. Initially, we performed laboratory adsorption experiments on an intact shale sample measuring 50 mm $\times$ 100 mm to obtain methane excess adsorption isotherms at 313.15, 333.15, and 353.15 K. Subsequently, to validate the accuracy of the spherical SLD model, we conducted regression analysis on the experimental data of the excess adsorption isotherms via the new model and compared it with several common adsorption theoretical models as well as the traditional slit and cylindrical SLD models. The effects of different pore structures (pore geometries, specific surface areas, diameters, and volumes) on the adsorption capacity and density distribution were also examined. Finally, this work investigates the impacts of different fluid-solid and fluid-fluid interactions on the adsorption behavior within shale pores. The objective of this study is to enhance our understanding of the gas adsorption mechanism within shale pores through the application of the newly developed spherical SLD model, thereby

facilitating the more effective utilization of SLD models in actual applications such as shale gas exploration.

2. Method

2.1. Spherical pores in nanoporous shale

The development and evolution of shale pore structure are controlled by three main factors: the total organic carbon content, mineral components, and thermal maturity (Fu et al., 2015). Among them, the pores generated within organic matter (OM) are considered to be the dominant contributors to the total porosity and oil-gas storage in organic-rich shale reservoirs (Löhr et al., 2015). Pores in OM usually form during the thermal maturation process when hydrocarbon substances are expelled from kerogen. Spherical pores, such as those due to asphalt and the bubbles within it, form during this process. Moreover, the formation of OM pores is closely related to the generation and development of spherical pores. First, only spotted spherical pores are formed within the OM and then gradually expand until they connect with each other, eventually forming a "pit" structure that is much larger than the surrounding pores. The shape and size of this structure are restricted by the OM or the internal mineral particle framework (Huang et al., 2020). Additionally, owing to the overpressure-associated overburden stress unloading in the gentle anticlines, spherical pores also form within the OM (Liu et al., 2020). In summary, spherical pores are widely present in the OM.

Owing to the greater curvature of the concave geometry, the contact area with gas molecules is increased. Compared with slit and cylindrical nanopores, spherical nanopores have a greater adsorption capacity (Li et al., 2023a; Qajar et al., 2016). Therefore, the adsorption characteristics of spherical pores can better represent the adsorption performance of nanopores within shale. To characterize the gas adsorption behavior within shale accurately, we consider establishing a gas adsorption model on the basis of the geometry of the spherical pores, as illustrated in Fig. 2. In this model, the gray region represents the shale matrix (the adsorbent), and the blue region represents the gas molecules (the adsorbate).

2.2. Spherical SLD model development

Owing to the complex structure at the junctions of spherical pores with slit and cylindrical pores, the gas molecules adsorbed in this area are simultaneously affected by the pore wall solid molecules of several geometric shapes pores, which makes it impossible to characterize the adsorption behavior of gas molecules in this area via the SLD theory. However, ignoring the connectivity of the spherical pores results in a slightly smaller overall excess adsorption capacity of the shale pores, this error is within an acceptable range. To study the gas adsorption mechanism within spherical pores, spherical pores must be extracted from the complex pore structure of shale. Therefore, we finally obtain an SLD adsorption model with a spherical pore geometry, as shown in Fig. 3. By sectioning the spherical pore SLD model along any radial direction, we assume that the resulting model consists of a single layer of solid molecules capable of adsorbing gas molecules. We analyze an arbitrary gas molecule within this framework. Here, D_s represents the diameter of the hollow region within the spherical pore (nm); R_s denotes the radius of this hollow region ($D_s = 2R_s$, nm); z is the distance between the center of a gas molecule and the inner surface of the spherical pore (nm); and $R_s - z$ signifies the distance from the center of the spherical pore to the center of the gas molecule (nm).

2.2.1. Principle of SLD theory

The SLD theory was proposed by applying the mean-field approximation theory to density functional theory. Therefore,

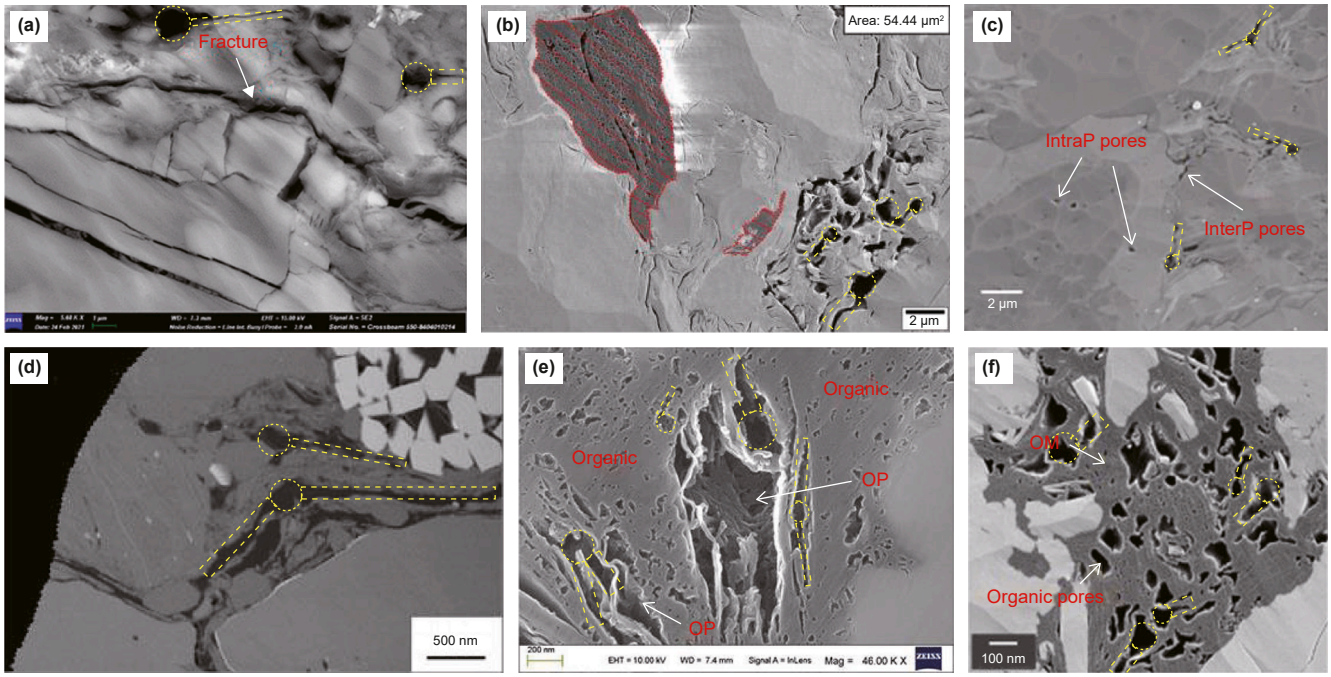

Fig. 1. FESEM images of the spherical nanopores in OM. Image (**a**) from Yin et al. (2022); image (**b**) from Gao et al. (2021); images (**c**) and (**f**) from Cao et al. (2019); image (**d**) from Zhao et al. (2022); and image (**e**) from Wang et al. (2021). The yellow circles represent spherical pores, which are connected to the slit or cylindrical pores indicated by the yellow dashed lines on both sides.

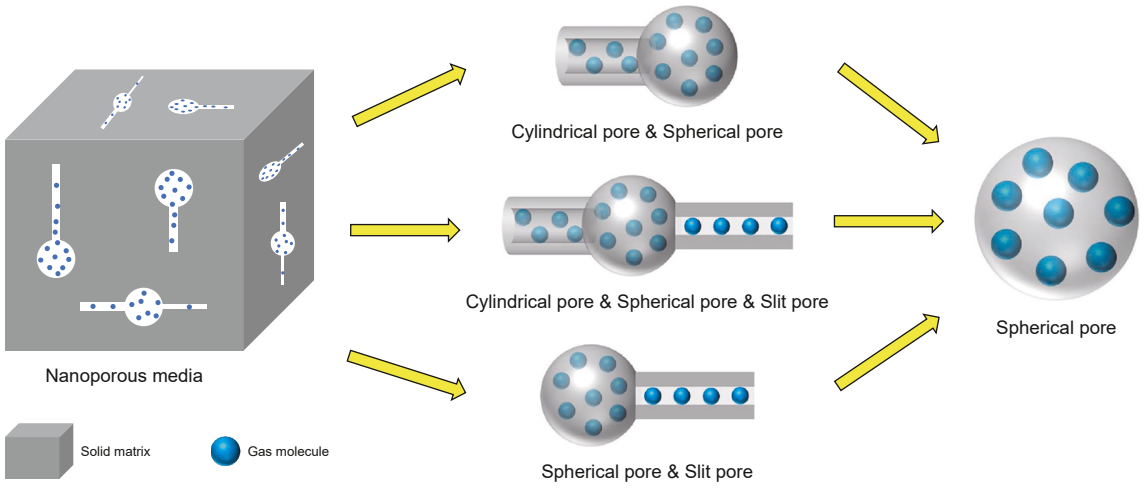

Fig. 2. Schematic diagram of different pore adsorption models.

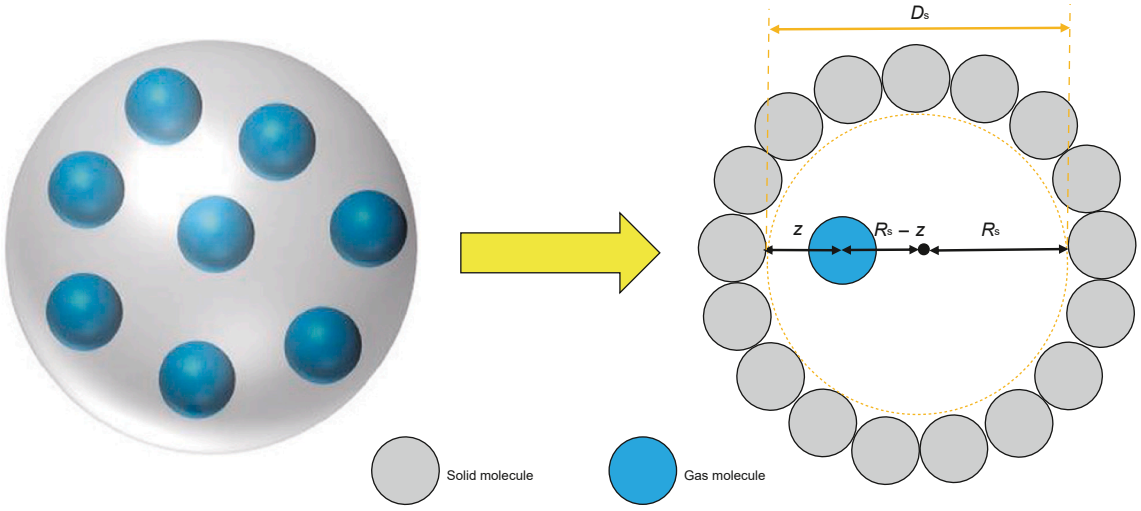

Fig. 3. Spherical pore SLD model.

this theory holds that when a fluid reaches adsorption equilibrium in space, there are no local chemical potential fluctuations, meaning that the chemical potentials at any position in space are equal. Specifically, for spherical pores in shale, the assumptions of the SLD theory are as follows: (1) the temperature and pressure distributions within the spherical pores are uniform; (2) all methane molecules and solid molecules of the pore wall, except those methane molecules in contact with the pore wall, are considered spherical; (3) the interaction between methane molecules and solid molecules of the pore wall is independent of temperature and the number of molecules; (4) the chemical potential at any position within the spherical pore is equal to that of the bulk phase; and (5) the chemical potential at any position within the spherical pore is the sum of the interactions between methane molecules and between methane molecules and solid molecules of the pore wall.

Therefore, when methane molecules reach adsorption equilibrium within the spherical pores, the chemical potential at any position within the pores is equal to the chemical potential of the bulk phase and is equal to the sum of the fluid-fluid and fluid-solid interaction potentials (Rangarajan et al., 1995).

$$\mu(z) = \mu_{\text{bulk}} = \mu_{\text{ff}}(z) + \mu_{\text{fs}}(z) \tag{1}$$

where $\mu(z)$ and μ_{bulk} represent the chemical potential at any position z within the spherical pore and in the bulk phase, respectively, J/mol. The $\mu_{\text{ff}}(z)$ and $\mu_{\text{fs}}(z)$ represent the chemical potential generated by the interaction between methane molecules of the pore and the interaction between methane molecules at position z and the solid molecules of the pore wall, respectively, J/mol. For real gases, μ_{bulk} and $\mu_{\text{ff}}(z)$ can be expressed in terms of fugacity as follows (Chen et al., 2018):

$$\mu_{\text{bulk}} = \mu_0(T) + RT \ln\frac{f_{\text{bulk}}}{f_0} \tag{2}$$

$$\mu_{\text{ff}}(z) = \mu_0(T) + RT \ln\frac{f_{\text{ff}}(z)}{f_0} \tag{3}$$

where $\mu_0(T)$ represents the chemical potential at any reference position, J/mol; f_{bulk} and $f_{\text{ff}}(z)$ represent the fugacity of the methane molecules in the bulk phase and the adsorbed phase at position z, respectively, in MPa; f_0 represents fugacity at any

position, MPa; R represents the gas constant, 8.314 J/(mol·K); and T represents the temperature within the spherical pore, K.

The chemical potential $\mu_{fs}(z)$, which quantifies the interaction between methane molecules and solid molecules within the pore wall, can be expressed as:

$$\mu_{fs}(z) = N_A\left[\psi^{fs}(z)\right] \tag{4}$$

where N_A is Avogadro's constant, 6.02 × 10^{23} mol^{-1}, and $\psi^{fs}(z)$ represents the potential energy function of the interaction between the methane molecules at position z and the solid molecules, J.

From Eqs. (1)–(4), the following adsorption equilibrium equation (Eq. (5)) can be obtained:

$$f_{ff}(z) = f_{bulk}\exp\left(\frac{\psi^{fs}(z)}{k_B T}\right) \tag{5}$$

where k_B denotes the Boltzmann constant, which is approximately 1.38 × 10^{-23} J/K.

2.2.2. Fluid-solid interaction (potential energy function)

Since the adsorption behavior of methane molecules in the spherical pores of shale is strongly influenced by the curvature of the spherical surface, it is necessary to select an appropriate potential energy function to characterize the interaction between methane molecules and the solid molecules on the pore wall accurately. Therefore, by integrating the Lennard-Jones 12−6 potential function along the spherical surface, we obtain the Lennard-Jones 10−4 potential function on the basis of the spherical surface in Eq. (6) and finally achieve an accurate calculation of the fluid-solid interaction potential energy at any position z within the spherical pores (Ravikovitch and Neimark, 2002; Siderius and Gelb, 2011; Baksh and Yang, 1991):

$$\psi^{fs}(z)_i = 2\pi\rho_s\varepsilon_{fs}\sigma_{fs}^2\left[\frac{2}{5}\sum_{k=0}^{9}\left(\frac{\sigma_{fs}^{10}}{R_{si}{}^k z_i{}^{10-k}} + (-1)^k\frac{\sigma_{fs}^{10}}{R_{si}{}^k (z_i - 2R_{si})^{10-k}}\right)\right.$$
$$\left. -\sum_{k=0}^{3}\left(\frac{\sigma_{fs}^{4}}{R_{si}{}^k z_i{}^{4-k}} + (-1)^k\frac{\sigma_{fs}^{4}}{R_{si}{}^k (z_i - 2R_{si})^{4-k}}\right)\right] \tag{6}$$

$$\varepsilon_{fs} = \sqrt{\varepsilon_{ss}\varepsilon_{ff}} \tag{7}$$

$$\sigma_{fs} = \frac{\sigma_{ss} + \sigma_{ff}}{2} \tag{8}$$

$$z_i = z + \left(i - \frac{1}{2}\right)\sigma_{ss} \tag{9}$$

$$R_{si} = R_s + \left(i - \frac{1}{2}\right)\sigma_{ss} \tag{10}$$

where ρ_s denotes the solid molecular density, 38.2 atoms/nm^2; ε_{ss}, ε_{ff} and ε_{fs} represent the solid-solid, fluid-fluid and fluid-solid interaction energy parameters, respectively, J; and σ_{ss} and σ_{ff} correspond to the diameters of the adsorbent and adsorbate molecules, nm. Importantly, the interaction potential between solid and gas molecules becomes negligible beyond the fourth layer (i.e., i = 4) of solid atoms. Consequently, the fluid-solid interaction potential $\psi^{fs}(z)$ within a spherical pore can be expressed as follows (Wang et al., 2022):

$$\psi^{fs}(z) = \sum_{i=1}^{4}\psi^{fs}(z)_i \tag{11}$$

2.2.3. Fluid-fluid interaction (fluid equation of state)

A suitable fluid equation of state (EOS) is of vital importance for understanding the physical and thermodynamic properties of fluids (Chabab et al., 2024). In this study, to describe the interactions between methane molecules accurately, we used the Peng-Robinson equation of state (PR-EOS), which can precisely characterize the density of methane gas under high-temperature and high-pressure conditions (Gasem et al., 2001). We also used this equation to calculate physical parameters such as the bulk phase density ρ_{bulk}, the bulk phase fugacity f_{bulk}, and the adsorbed phase fugacity $f_{ff}(z)$ of methane molecules in the pores accurately.

$$\frac{P}{\rho_{bulk}RT} = \frac{1}{1 - b\rho_{bulk}} - \frac{a\rho_{bulk}}{RT\left[1 + \left(1 - \sqrt{2}\,b\rho_{bulk}\right)\right]\left[1 + \left(1 + \sqrt{2}\,b\rho_{bulk}\right)\right]} \tag{12}$$

$$a = 0.457535c(T)R^2T_c^2\Big/P_c \tag{13}$$

$$b = 0.077796RT_c/P_c \tag{14}$$

where P represents pressure, MPa; ρ_{bulk} represents the bulk phase density, mol/m^3; a represents the attractive parameter in the bulk phase, J·m^3/mol^2; b represents the repulsive parameter in the bulk phase, m^3/mol; P_c represents the critical pressure, MPa; and T_c represents the critical temperature, K. $c(T)$ represents the dependence of the attractive parameter a on temperature, which can be expressed by the following function:

$$c(T) = \left[1 + C_1\left(1 - \sqrt{\frac{T}{T_c}}\right) + C_2\left(1 - \sqrt{\frac{T}{T_c}}\right)^2 + C_3\left(1 - \sqrt{\frac{T}{T_c}}\right)^3\right]^2 \tag{15}$$

where C_1 to C_3 represent the regression parameters, and the physical property parameters of methane are shown in Table 1.

On the basis of PR-EOS, the fugacity f_{bulk} of gas molecules in the bulk phase can be expressed as:

$$\ln\frac{f_{bulk}}{P} = \frac{b\rho_{bulk}}{1 - b\rho_{bulk}} - \frac{a\rho_{bulk}}{RT\left(1 + 2b\rho_{bulk} - b^2\rho_{bulk}^2\right)} - \ln\left[\frac{P}{RT\rho_{bulk}} - \frac{Pb}{RT}\right]$$
$$-\frac{a}{2\sqrt{2}RT}\ln\left[\frac{1 + \left(1 + \sqrt{2}\right)b\rho_{bulk}}{1 + \left(1 - \sqrt{2}\right)b\rho_{bulk}}\right] \tag{16}$$

Furthermore, the adsorbed phase fugacity $f_{ff}(z)$ of gas molecules at position z can also be represented as:

Table 1
Physical property parameters of methane.

Fluid	P_c, MPa	T_c, K	σ_{ff}, nm	ε_{ff}/k_B, K	C_1	C_2	C_3
CH_4	4.599	190.56	0.3730	148.0	0.41108	−0.14020	0.27998

$$\ln\frac{f_{ff}(z)}{P}=\frac{b_{ads}\rho(z)}{1-b_{ads}\rho(z)}-\frac{a_{ads}(z)\rho(z)}{RT\left(1+2b_{ads}\rho(z)-b_{ads}^2\rho^2(z)\right)}-\ln\left[\frac{P}{RT\rho(z)}-\frac{Pb_{ads}}{RT}\right]-\frac{a_{ads}(z)}{2\sqrt{2}RT}\ln\left[\frac{1+\left(1+\sqrt{2}\right)b_{ads}\rho(z)}{1+\left(1-\sqrt{2}\right)b_{ads}\rho(z)}\right] \tag{17}$$

where $\rho(z)$ represents the gas adsorbed phase density at position z from the wall surface within the spherical pore, mol/m^3; $a_{ads}(z)$ is the attractive parameter in the adsorbed phase, J·m^3/mol^2; and b_{ads} is the repulsive parameter in the adsorbed phase, m^3/mol. The detailed solution process of the attractive parameter $a_{ads}(z)$ in the adsorbed phase is provided in the appendix. The repulsive parameter b_{ads} in the adsorbed phase can be obtained by introducing the covolume correction parameter Λ_b into the repulsive parameter b in the bulk phase, and its expression is as follows:

$$b_{ads}=b(1+\Lambda_b) \tag{18}$$

In conclusion, after calculating the adsorbed phase density $\rho(z)$ on the basis of the adsorption equilibrium criterion in Eq. (5), we finally present the expression for the excess gas adsorption amount on the basis of the density distribution within spherical pores:

$$\Gamma^{ex}=4\pi\int_{3\sigma_{ff}/8}^{R_s}(R_s-z)^2[\rho(z)-\rho_{bulk}]dz \tag{19}$$

where Γ^{ex} is the excess adsorption capacity, mmol/g.

The specific calculation process of the spherical SLD adsorption model proposed in this study is shown in Fig. 4. First, we calculate the fluid-solid interaction potential $\psi^{fs}(z)$ in spherical pores via the Lennard-Jones 10–4 potential function. Moreover, the density ρ_{bulk} and fugacity f_{bulk} of the bulk phase were obtained via PR-EOS. We subsequently divided half of the spherical pores into 50 parts and calculated the fugacity $f_{ff}(z)$ and density $\rho(z)$ of the adsorbed phase in each part successively starting from the position close to the pore wall until the adsorption equilibrium conditions were met in each part. Finally, the excess adsorption capacity Γ^{ex} was calculated by writing the Simpson formula related code via MATLAB software.

3. Results and analysis

3.1. Shale samples and experimental methods

3.1.1. Experimental samples

The sample utilized in this study is the shale from the Longmaxi Formation in Sichuan Province, sourced from the Sichuan Basin, which possesses the richest known shale gas reserves in China. Typically, shale adsorption tests recommend crushing a shale sample into powder for analysis. However, this process can lead to alterations in the original pore structure of the sample, such as crack expansion, pore collapse, and increased surface area, all of which may affect the sample's adsorption capacity (Liu et al., 2012, 2021). To preserve the original pore structure as much as possible, avoiding reductions in the number of spherical pores or increases in the number of slit pores, we employed intact cylindrical shale samples with dimensions of 50 mm × 100 mm for the adsorption tests.

3.1.2. Experimental equipment

The adsorption test employs the volumetric method to quantify changes in gas pressure, thereby determining the amount of methane adsorbed in shale samples. The testing apparatus is a BRXF-II high-temperature and high-pressure isothermal adsorption instrument manufactured by Jiangsu Boruisi Scientific Research Instrument Co., Ltd. As illustrated in Fig. 5, this equipment comprises a computer control and data acquisition system, a gas supply system, an adsorption testing system, and a waste gas collection system. The pressure sensor has an accuracy of 0.001 MPa, whereas the temperature sensor has an accuracy of 0.1 °C. Prior to conducting the adsorption test, to minimize the impact of moisture on the adsorption results, the shale samples were dried in an oven at 105 °C for 48 h until the quality of the samples remained unchanged. Additionally, further drying and vacuuming were performed at the experimental temperature for 3 h. Ultimately, methane adsorption isotherms with a purity of 99.999% were obtained at temperatures of 313.15, 333.15, and 353.15 K and pressures ranging from 0.8 to 14 MPa.

3.2. Verification of the accuracy and rationality of the spherical SLD adsorption model

This section aims to validate the accuracy and applicability of the spherical SLD model via shale adsorption experimental data obtained at different temperatures. Furthermore, the spherical SLD model was compared with commonly employed adsorption models, including the Langmuir, BET, O-K, D-R, F-A and modified D-A models, in terms of their fitting performance against the experimental data. The rationality and practicality of the new SLD model were evaluated through this comparative analysis. Additionally, the average absolute deviation (%AAD) and coefficient of determination (R^2) were utilized as metrics to assess the deviation between the calculated results and experimental data, as well as the goodness of fit of the models.

3.2.1. Experimental adsorption isotherms were characterized via the spherical pore SLD model

Several excess adsorption isotherms, which characterize the adsorption capacity of shale at various temperatures, were obtained from laboratory adsorption experiments. A comparison between these experimental results and the calculated outcomes of the spherical SLD model is presented in Fig. 6. The excess adsorption capacity is positively correlated with increasing gas pressure. This phenomenon can be attributed to the fact that higher pressure leads to a significant increase in the number of gas molecules entering the pore bulk phase, thereby shifting the adsorption equilibrium within the pores towards reducing the concentration of bulk phase molecules. This results in an increased discrepancy between the concentration of the adsorbed phase near the pore walls and the concentration of the bulk phase. However, when the pressure reached approximately 8–12 MPa, the excess adsorption capacity peaked and subsequently began to decrease. This decrease can be attributed to the full occupation of adsorption sites on the pore surface by methane molecules, leading to a reduction in the overall surface energy and, consequently, a gradual decrease in the adsorption capacity. Furthermore, there is a negative correlation between temperature and adsorption capacity; as temperature increases, the adsorption capacity decreases. Specifically, the maximum adsorption capacity was observed at 0.0375 mmol/g at 313.15 K, which decreased to 0.0336 mmol/g at 333.15 K and further decreased to 0.0305 mmol/g at 353.15 K. This trend was due to the increase in internal system energy with increasing temperature, causing the adsorption equilibrium to shift toward lower internal energy states. Given that adsorption is an exothermic process while desorption is endothermic, the reduction in system internal energy results in a higher desorption rate than the adsorption rate. Consequently, the

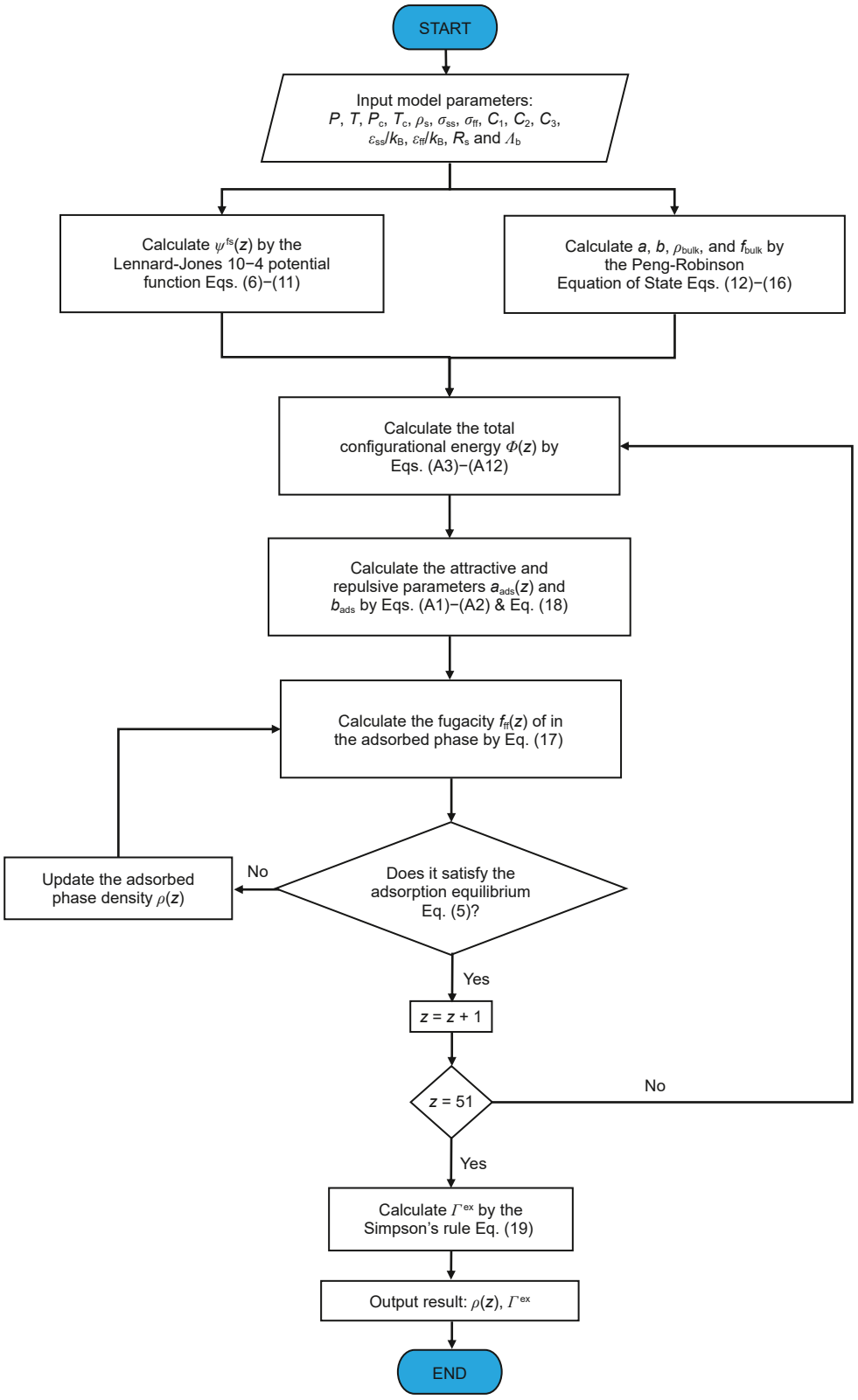

Fig. 4. Calculation flowchart of the spherical SLD adsorption model.

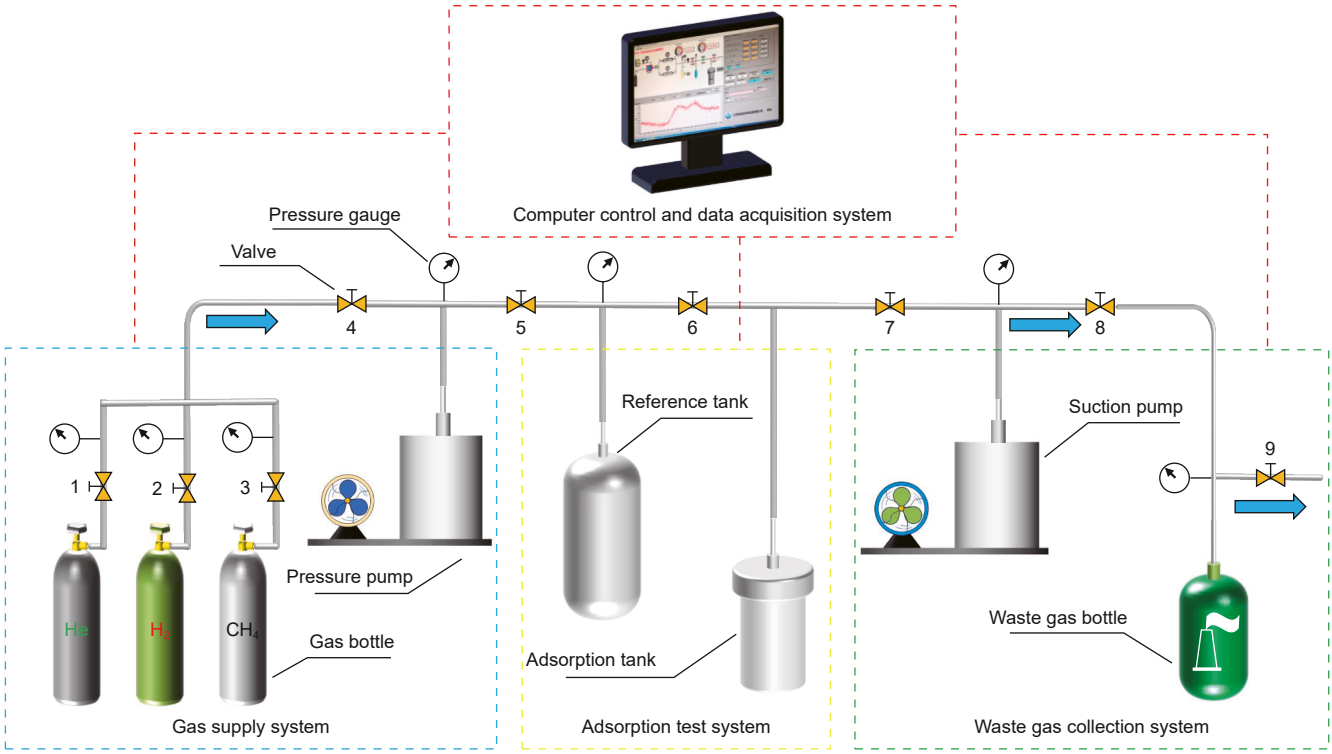

Fig. 5. Composition of the adsorption experimental equipment.

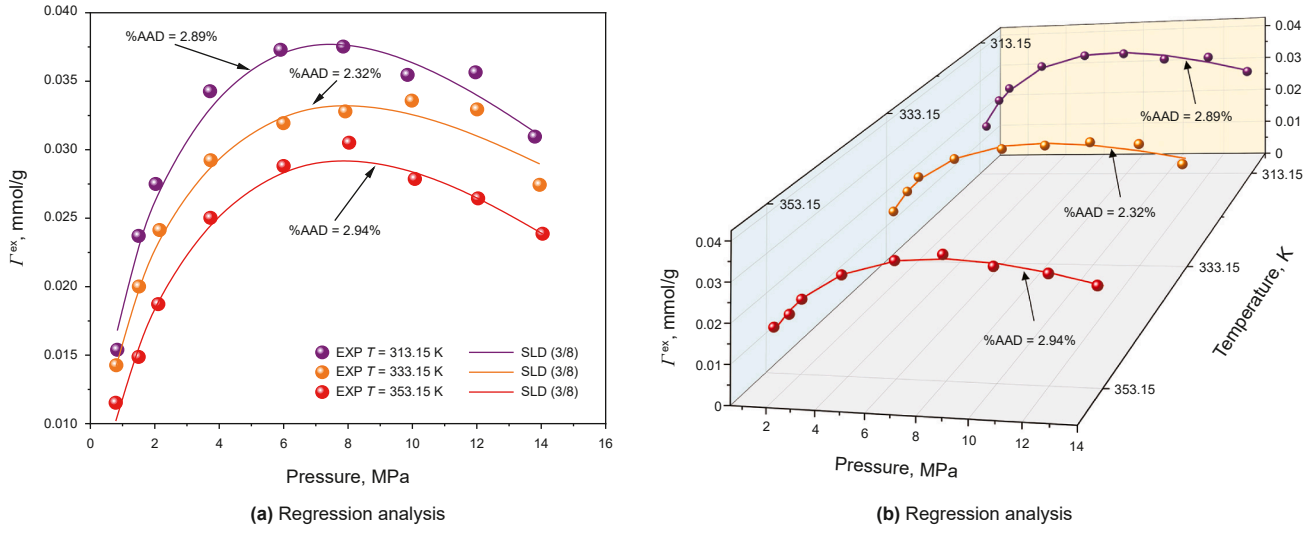

(a) Regression analysis **(b)** Regression analysis

Fig. 6. The methane excess adsorption isotherms at different temperatures were obtained via laboratory adsorption experiments and the spherical SLD model.

internal energy is converted into molecular kinetic energy through heat absorption, leading to the continuous escape of gas molecules from the adsorbed phase until the system re-establishes equilibrium.

The %AAD used in this study to verify the degree of data bias is defined as:

$$\%AAD = \frac{1}{N_p}\sum_{i=1}^{N_p}\left|\frac{n_{EXP} - n_{SLD}}{n_{EXP}}\right| \times 100\% \quad (20)$$

In this study, N_p denotes the number of data points obtained from both the laboratory experiment and the SLD model, whereas n_{EXP} represents the data derived from the laboratory adsorption experiment. Additionally, n_{SLD} signifies the outcome of the spherical SLD model calculations. As illustrated in Fig. 6, the results calculated via the newly developed SLD model exhibit excellent agreement with the experimental adsorption data, demonstrating minimal average absolute error values. Specifically, at temperatures of 313.15, 333.15, and 353.15 K, the average absolute deviations are 2.89%, 2.32%, and 2.94%, respectively, with an overall mean of 2.72%. The newly established SLD model demonstrates high precision in characterizing the adsorption behavior of shale across various temperatures. Furthermore, on the basis of the experimental adsorption data obtained at 333.15 K, we conducted

a comparative analysis of the spherical SLD model using the (1/2) σ_{ff} and (3/8) σ_{ff} hypotheses. The comparison results are presented in Fig. 7. The average absolute deviations for these two methods were 4.33% and 2.32%, respectively. Clearly, the SLD model assuming (3/8) σ_{ff} yielded results that more closely matched the experimental data. The research results are similar to those of Zeng et al. (2024), Wu et al. (2022), and Zeng et al. (2021). They reported that the pore space under the (1/2) σ_{ff} assumption is smaller than that under the (3/8) σ_{ff} assumption, which leads to the exclusion of some fluid molecules that interact with specific molecules. Furthermore, it has an impact on the accuracy of describing the actual excess adsorption amount and adsorbed phase density in the pores. The (3/8) σ_{ff} hypothesis is more acceptable than the (1/2) σ_{ff} hypothesis. Consequently, the spherical pore SLD model based on the (3/8) σ_{ff} hypothesis is better suited for characterizing the adsorption behavior of shale and will be further discussed below.

3.2.2. Comparison between the spherical SLD model and conventional adsorption theory models

In general, the adsorption behavior of most adsorbents can be described via conventional theoretical adsorption models. However, the actual temperature and pressure conditions within underground shale reservoirs significantly exceed the critical temperature (190.56 K) and critical pressure (4.599 MPa) of methane, indicating that methane adsorption by shale occurs under supercritical conditions. The quantity of methane adsorbed onto the shale surface initially increases with increasing pressure but subsequently decreases as the pressure continues to rise. Consequently, it is imperative to adapt conventional adsorption models for supercritical conditions. According to Gibbs's definition, the following conversion relationship exists between the excess adsorption amount and the absolute adsorption amount (Gasparik et al., 2014a, 2014b).

$$V_{exc} = V_{abs}\left(1 - \frac{\rho_g}{\rho_a}\right) \tag{21}$$

where V_{exc} denotes the excess adsorption amount and V_{abs} represents the absolute adsorption amount. Here, ρ_g signifies the bulk phase density, and ρ_a indicates the adsorbed phase density. By substituting the absolute adsorption capacity from Eq. (21) into the conventional adsorption model, we derive a supercritical adsorption model represented by the excess adsorption capacity, as illustrated in Eqs. (22)–(27). Eq. (22) is the supercritical Langmuir model (Xiong et al., 2021). Eq. (23) is the supercritical BET model (Zhou et al., 2019). Eq. (24) is the supercritical O-K model (Bi et al., 2016). Eq. (25) is the supercritical D-R model (Sakurovs et al., 2007). Eq. (26) is the supercritical F-A model (Li et al., 2023b). Eq. (27) is the modified D-A model (Jakubov and Mainwaring, 2002).

$$V_{exc} = \frac{V_{max} V_L P}{1 + V_L P}\left(1 - \frac{\rho_g}{\rho_a}\right) \tag{22}$$

$$V_{exc} = \frac{V_{max} C P}{\left(P^0 - P\right)\left[1 + (C-1)\left(\frac{P}{P^0}\right)\right]}\left(1 - \frac{\rho_g}{\rho_a}\right) \tag{23}$$

$$V_{exc} = \frac{2V_{max}\rho_g\left[1 - \exp\left(\frac{\varepsilon_{fs}}{k_B T}\right)\right]}{\frac{\rho_g\rho_a}{\rho_a - \rho_g} + \rho_a \exp\left(\frac{\varepsilon_{fs}}{k_B T}\right)}\left(1 - \frac{\rho_g}{\rho_a}\right) \tag{24}$$

$$V_{exc} = V_{max}\exp\left\{-H\left[\ln\left(\frac{P^0}{P}\right)\right]^2\right\}\left(1 - \frac{\rho_g}{\rho_a}\right) \tag{25}$$

$$V_{exc} = F\left[\ln\left(\frac{P^0}{P}\right)\right]^{\frac{D-3}{3}}\left(1 - \frac{\rho_g}{\rho_a}\right) \tag{26}$$

$$V_{exc} = V_{max}\exp\left\{-H\left[\ln\left(27\left(\frac{P^0}{P}\right)^{1/3} + 9\left(\frac{P^0}{P}\right)^{1/2} + 3\frac{P^0}{P} + 1\right)\right]\right\}\left(1 - \frac{\rho_g}{\rho_a}\right) \tag{27}$$

where V_{max} represents the maximum absolute adsorption capacity, mmol/g; V_L denotes the Langmuir constant, MPa^{-1}; and both C and H are constants associated with the heat of adsorption. Additionally, D signifies the fractal dimension, whereas F is a constant. Given that methane adsorption on the shale surface occurs in a supercritical state, the liquefaction of methane is not feasible under these conditions. Therefore, P^0 in this context refers to the hypothetical saturated vapor pressure (in MPa) (Amankwah and Schwarz, 1995).

As illustrated in Fig. 8, when multiple adsorption models were employed to fit the experimental data from this study, the SLD, Langmuir, D-R and modified D-A models exhibited superior fitting performance, with R^2 values exceeding 0.97. These findings indicate that the SLD model can be used to characterize the methane gas adsorption behavior in shale pores, and the characterization accuracy is relatively high. However, unlike the SLD model, other adsorption models yield primarily empirical parameters when fitted to methane adsorption data. These parameters typically cannot be directly correlated with fundamental shale characteristics such as pore geometries, specific surface areas, diameters, and volumes. Additionally, while these models adequately describe the adsorption behavior of shale, they fail to accurately differentiate between the densities of the adsorbed phase and bulk phase, which should vary with increasing gas pressure but are treated as constants in these models. In contrast, the SLD model not only correlates various adsorbent properties such as pore geometries, specific surface areas, diameters and volumes but also, effectively characterizes the distribution of gas density within

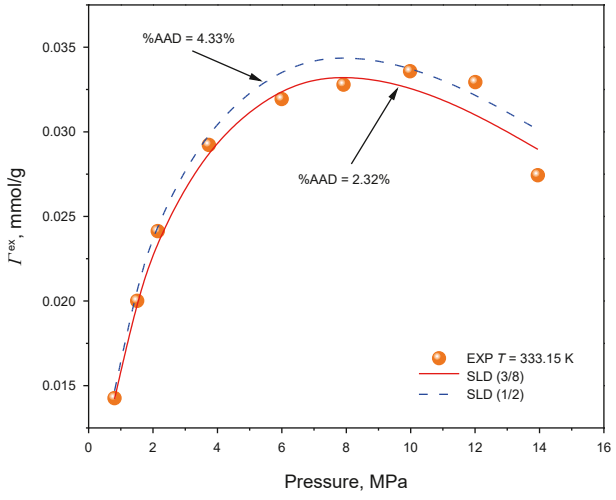

Fig. 7. Comparison of the (1/2) σ_{ff} hypothesis with the (3/8) σ_{ff} hypothesis.

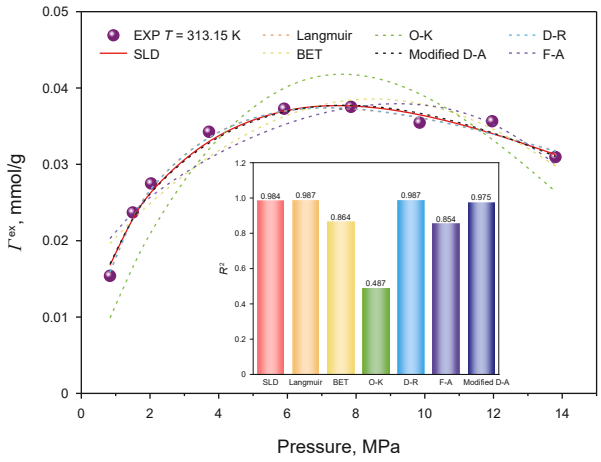

Fig. 8. Comparison of SLD with conventional adsorption theoretical models and its R^2.

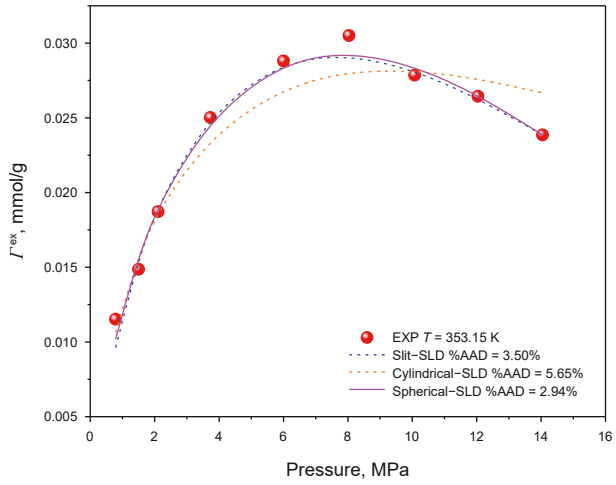

Fig. 9. Comparison of the spherical, slit and cylindrical SLD models for characterizing laboratory excess adsorption isotherms at 353.15 K.

pores, thereby providing a more comprehensive understanding of shale gas occurrence in shale pores.

4. Adsorption mechanism of shale based on the spherical SLD model

A significant advantage of the SLD theory is that it can combine the intricate pore structure of nanoporous shale with gas adsorption behavior. Therefore, in this section, spherical, slit and cylindrical pore SLD models are first compared to analyze the influences of different pore geometries and pore sizes on adsorption. Second, the influences of different fluid-solid interactions and different fluid-fluid interactions on the adsorption behavior in spherical pores are investigated.

4.1. Comparison and analysis of the spherical, slit and cylindrical SLD models

As a heterogeneous material with pronounced anisotropic properties, shale has abundant nanopores and intricate pore structures, including slit, cylindrical, and spherical pores. These features significantly complicate the adsorption behavior of methane. To gain deeper insights into the adsorption characteristics of shale and the distribution of methane molecules within nanopores, we employed slit, cylindrical, and spherical pore SLD models to characterize laboratory adsorption isotherms at 353.15 K and systematically compared and analyzed the corresponding density distribution profiles. The fitting parameters for the three SLD models are summarized in Table 2, where the slit and cylindrical SLD models each have four fitting parameters, whereas the spherical SLD model has only three.

Fig. 9 shows that the calculated results from several models exhibit a high degree of consistency with the adsorption isotherm data. Compared with the traditional slit and cylindrical SLD models, the newly established spherical SLD model better fits the laboratory adsorption data, and its average absolute deviation is 2.94%, whereas the average absolute deviations of the slit and cylindrical SLD models are 3.5% and 5.65%, respectively. In the regression analysis of the adsorption isotherms, the number of fitting parameters significantly influences the SLD model. The values of these parameters are iteratively adjusted to increase the fitting accuracy. However, an excessive number of fitting parameters can complicate both computation and interpretation, whereas an insufficient number may compromise fitting performance. To address this challenge, the new model refines the traditional 4−parameter SLD model into a 3−parameter version, thereby reducing complexity and enhancing fitting precision.

Fig. 10 shows the absolute adsorption density distributions derived from laboratory adsorption isotherms at 353.15 K via the three models. The horizontal axis denotes the distance between the center of any fluid molecule and the pore wall, with the figure displaying only the density distribution within half of the pore area. The red regions signify areas of strong adsorption, the green regions indicate areas of weak adsorption, and the blue regions represent the bulk phase.

As shown in Fig. 10, the adsorption density distributions of the three SLD models exhibit a consistent trend. Under constant pressure, the molecular density increases as the distance from the pore wall decreases and decreases as the distance from the pore wall increases. This phenomenon can be attributed to the stronger interaction between fluid molecules and solid molecules on the pore surface when they are closer to the pore wall, resulting in a high-density adsorption zone. Conversely, the weakening of fluid-solid interactions at greater distances from the pore wall leads to a gradual decrease in density, ultimately forming the bulk phase region. As the pressure begins to rise, the overall density also increases; however, the rate of increase diminishes with increasing pressure. This behavior is due to the increased occupation of adsorption sites on the pore surface by gas molecules as the pressure increases.

Furthermore, the density distributions of the three SLD models exhibit significant differences. Despite characterizing laboratory adsorption isotherms at the same temperature, the maximum adsorbed phase densities for the slit, cylindrical, and spherical SLD models were 11300, 16900, and 12100 mol/m^3, respectively, with the cylindrical model exhibiting the highest density, followed by the spherical model and then the slit model. These variations are

Table 2
Input parameters of the spherical, slit and cylindrical SLD models used to characterize the laboratory excess adsorption isotherms at 353.15 K.

Parameters / SLD model	ε_{fs}/k_B, K	R_s, nm	L_s, nm	A_s, m^2/g	Λ_b	%AAD, %
Slit pore	14.57	—	0.88	14.12	0.94	3.5
Cylindrical pore	16.73	0.72	4.52	—	0.47	5.65
Spherical pore	4.85	1.49	—	—	0.64	2.94

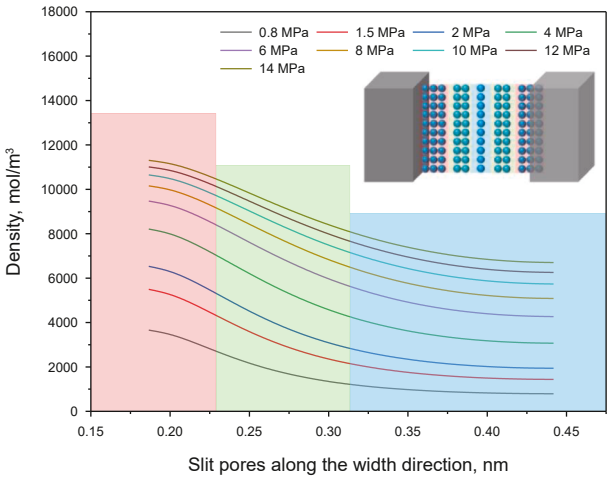

(a) Slit SLD model

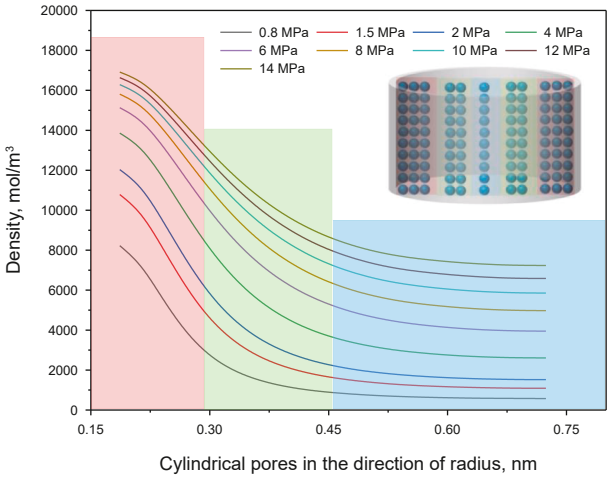

(b) Cylindrical SLD model

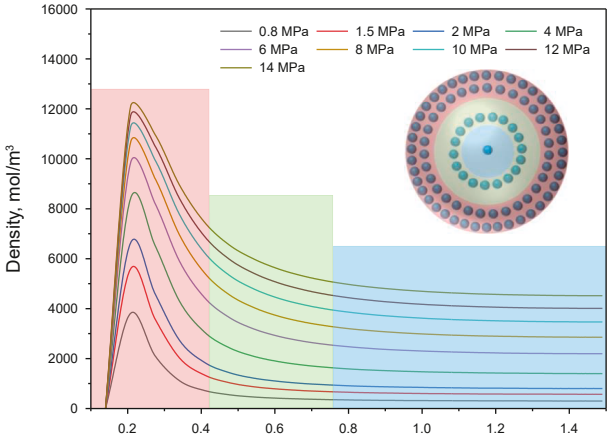

(c) Spherical SLD model

Fig. 10. The distribution characteristics of the absolute adsorption density in the laboratory were characterized by slit, cylindrical and spherical SLD models (the density distribution in the figure shows only the 1/2 pore size range).

attributed primarily to the differences in internal volume and surface area among the different pore geometries. Additionally, under identical pressure conditions, the rate of change in the adsorption density varies among the three models. Specifically, the spherical SLD model results in the most rapid density change, whereas the slit SLD model results in the slowest change. Moreover, within spherical pores, the density does not peak at (3/8) σ_{ff} but rather reaches its maximum at approximately (3/5) σ_{ff} because of the pronounced curvature of the inner pore walls. This curvature leads to an uneven distribution of fluid molecules, resulting in more rapid density changes and a delayed peak value.

4.2. Comparison and analysis of SLD models with different geometries

The specific surface area of pores is a critical parameter influencing the adsorption behavior in shale. Consequently, when the pore size and volume are held constant, variations in pore geometry result in differing specific surface areas, which significantly impact the gas adsorption capacity. To further investigate the influence of pore structure on the adsorption capacity of nanoporous shale, slit, cylindrical, and spherical SLD models were used to calculate the methane adsorption capacity and density distribution at 353.15 K. The parameters employed in these calculations are detailed in Table 3. To ensure consistency in pore size and volume across the three geometries, we standardized the pore diameter to 2 nm and the pore volume to $4\pi/3$ nm^3. This standardization resulted in specific surface areas of $4\pi/3$ m^2/g for slit pores, $8\pi/3$ m^2/g for cylindrical pores, and $12\pi/3$ m^2/g for spherical pores. All other parameters from the preceding section were maintained at their average values.

Fig. 11 shows the adsorption isotherms derived from the SLD models with varying pore geometries. Under identical pore size and volume conditions, the specific surface area of cylindrical pores is twice that of slit pores, whereas the specific surface area of spherical pores is threefold greater than that of slit pores. Consequently, the maximum excess adsorption capacity in cylindrical pores exceeds that in slit pores by more than twofold, and in spherical pores, it surpasses that in slit pores by more than fourfold. These findings indicate a significant influence of the pore specific surface area on the adsorption capacity, demonstrating that the adsorption capacity increases proportionally with the specific surface area. Fig. 12 shows the distributions of the absolute density as calculated via various models. While there is no apparent correlation between density and either specific surface area or adsorption capacity, the maximum density has the following relationship: spherical model > cylindrical model > slit model. Furthermore, under low-pressure conditions, the disparity between the maximum density adjacent to the spherical pore wall and that near the walls of other shapes is more pronounced than

Table 3
Input parameters of the spherical, slit and cylindrical pore SLD models with the same pore size.

Parameters / SLD model	ε_{fs}/k_B, K	R_s, nm	L_s, nm	A_s, m^2/g	Λ_b	V_{max}, mmol/g
Slit pore	12	—	2	$4\pi/3$	0.7	0.00393
Cylindrical pore	12	1	4/3	$8\pi/3$	0.7	0.00843
Spherical pore	12	1	—	$12\pi/3$	0.7	0.01892

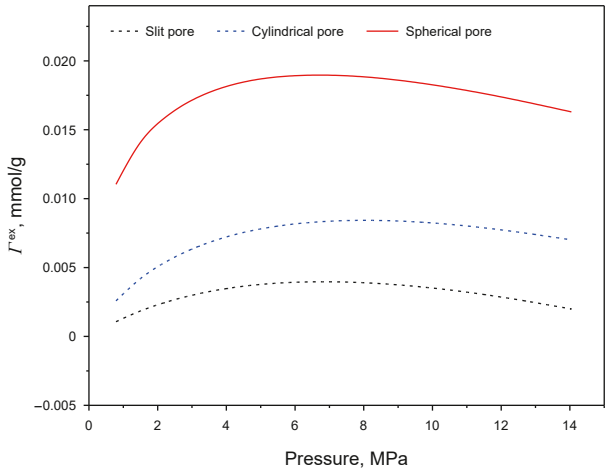

Fig. 11. Influence of different pore geometries on the excess adsorption isotherms.

that under high-pressure conditions. This phenomenon can be attributed to the greater specific surface area of the spherical pores, which enhances the fluid-solid interaction energy, thereby facilitating a higher concentration of gas molecules adsorbed near the pore wall at lower pressures.

Notably, the gas adsorption capacity and density distribution characteristics are significantly influenced by the pore specific surface area, whereas parameters such as specific surface area and volume are intrinsically linked to the pore geometry. Consequently, neglecting pore geometry can lead to substantial inaccuracies in predicting and characterizing the adsorption behavior of shale.

4.3. Comparison and analysis of the spherical SLD models with different pore sizes

To investigate the impact of varying pore sizes on the adsorption behavior within the shale spherical pores, the parameters $\varepsilon_{fs}/k_B = 4.85$ K and $\Lambda_b = 0.64$ were utilized to construct a spherical SLD model with diameters D_s ranging from 1, 1.5, and 2 to 10 nm in 1 nm increments. The excess adsorption isotherms at 353.15 K were subsequently calculated, as illustrated in Fig. 13.

The excess adsorption capacity refers to the difference in the amount of gas between the case where adsorption occurs in any given volume of pores and the case where it does not occur. It is also equal to the numerical integration along the radial direction of the difference between the adsorbed phase density near the pore walls and the bulk phase density at the center of the pores, as shown in Eq. (19). As shown in Fig. 13, when the aperture size remains unchanged, the excess adsorption amount in the pores tends to increase first and then decrease with increasing pressure. When the aperture size is less than 8 nm, the maximum excess adsorption amount in the pores increases with increasing aperture size; when the aperture size is approximately 8 nm, the maximum excess adsorption amount no longer increases significantly; and when the aperture size is greater than 8 nm, the maximum excess adsorption amount decreases with increasing aperture size. In addition, under high pressure, the maximum excess adsorption amount in the pores can gradually become negative. This is because when the pore diameter is less than 8 nm, the adsorbed phase density and bulk phase density both increase at the same rate with increasing pressure. At this time, the influence on the excess adsorption amount is relatively small; however, when the pore diameter reaches approximately 8 nm, because many

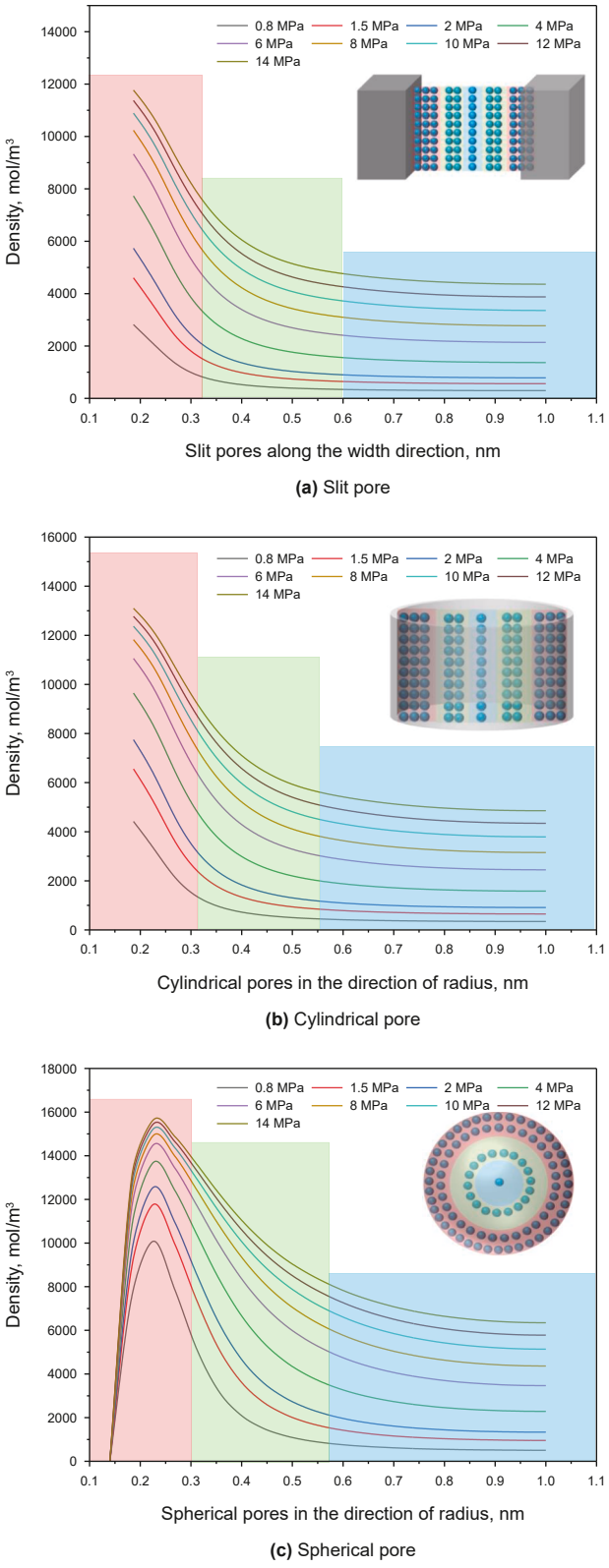

Fig. 12. Characteristics of the density distributions in various pore geometries.

effective adsorption sites in the adsorbed phase near the pore wall are occupied by methane molecules, the adsorbed phase density basically remains unchanged as the pressure increases, whereas the bulk phase density in the pore center continuously increases at

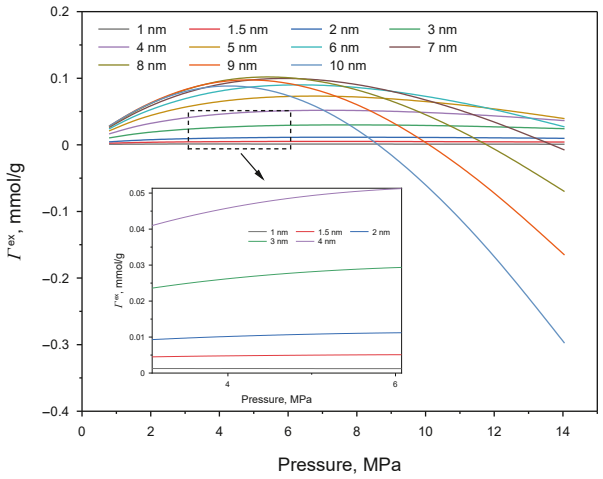

Fig. 13. Excess adsorption isotherms in the spherical SLD model for different pore diameters.

a relatively fast rate with increasing pressure, resulting in the cessation of the increase in the excess adsorption amount. Especially under high pressure, when the bulk phase density is large enough, the excess adsorption amount can change from a positive value to a negative value. This phenomenon is consistent with the research results obtained by Song et al. (2018) and Myers and Monson (2002).

A variety of spherical SLD models have been developed with varying pore sizes. In this study, we focus on models with diameters of 2, 5, and 10 nm to analyze their density distributions. Fig. 14 shows the density distributions calculated via the spherical SLD model for the specified pore sizes. The results indicate that the maximum adsorbed phase densities are 12,650, 10,870, and 6,840 mol/m^3. As the pore diameter increases, the maximum adsorbed phase density tends to decrease. This trend can be attributed to the increased distance between fluid molecules and solid surface molecules within the pores, leading to a reduction in the interaction energy. Consequently, more fluid molecules gradually move away from the adsorbed phase. Additionally, when the adsorbed phase density is below 5,170 mol/m^3 at maximum pressure, the excess adsorption amount becomes negative, further supporting the aforementioned observations. In addition, the adsorbed phase density in the 2, 5 and 10 nm spherical pores reached its peak at 0.226, 0.258 and 0.383 nm from the pore wall. With increasing pore diameter, the position where the maximum adsorbed phase density is reached is farther from the pore wall. This phenomenon can be attributed to the interaction between solid molecules and adsorbed fluid molecules on the pore surface. In pores with smaller diameters, the interaction between solid and fluid molecules typically predominates. However, in larger pores, the interactions among fluid molecules themselves become more significant (Zaitseva and Tovbin, 2023).

4.4. Influence of different fluid-solid interactions on the adsorption of the spherical SLD model

The number of layers of solid molecules on the pore wall significantly influences the capacity of the adsorbent to adsorb gas molecules. In traditional slit and cylindrical pore SLD models, the layer number of solid molecules is typically set to four when calculating the potential energy of fluid-solid interactions; however, previous studies (Rangarajan et al., 1995; Chen et al., 1997) have not provided a detailed rationale for this choice.

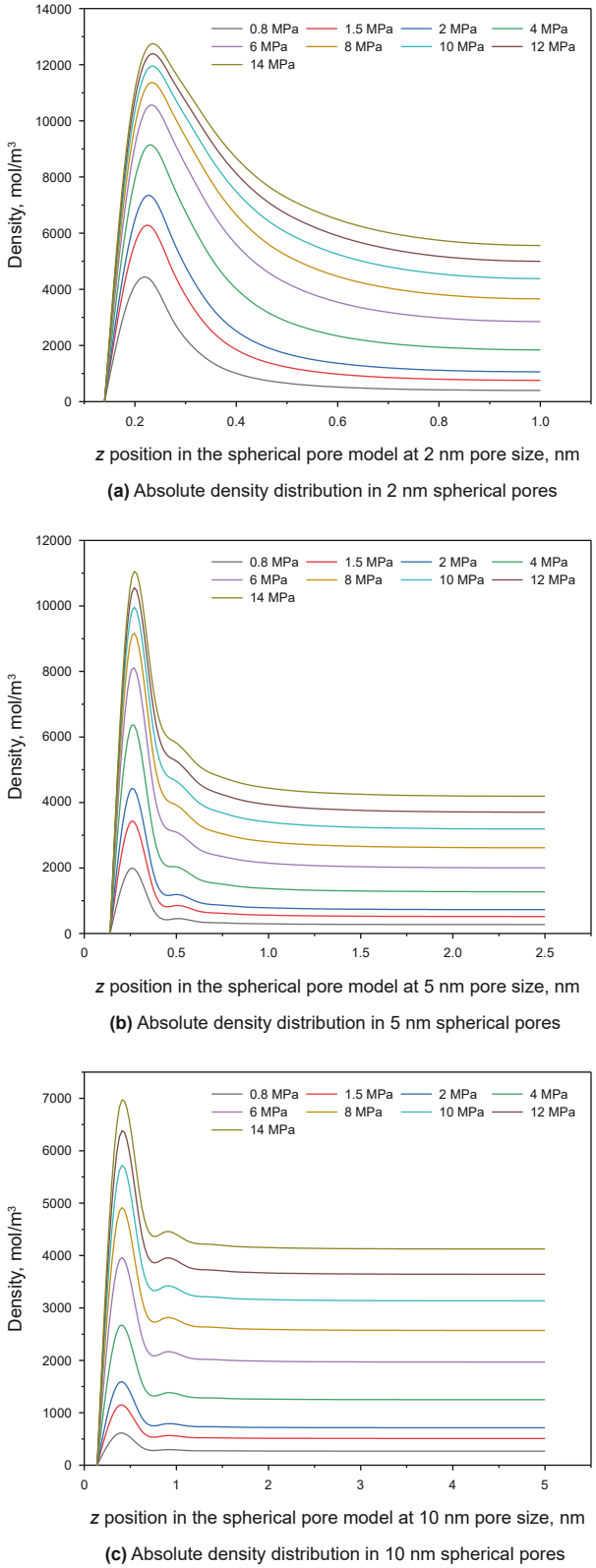

Fig. 14. Absolute density distributions of the spherical SLD model for different pore sizes.

Consequently, this section aims to compare and analyze the adsorption behavior of the spherical SLD model by varying the number of solid molecular layers. Furthermore, we validated the optimal number of solid molecular layers.

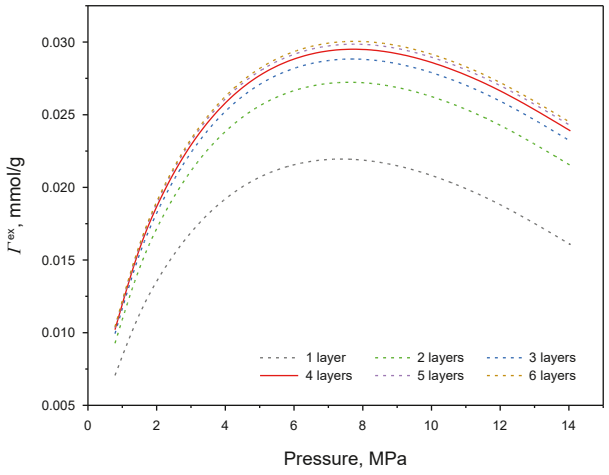

Fig. 15. Adsorption isotherms of the spherical SLD model with different numbers of solid molecular layers.

As shown in Fig. 15, for spherical pore adsorption isotherms with different pore wall molecular layers, the fourth molecular adsorption isotherm can obviously serve as a dividing line. Before the fourth layer, the adsorption isotherms from the first layer to the fourth layer clearly differ, among which the %AAD values of the adsorption isotherms from the first layer to the fourth layer are 39.25% and 9.18% between the second and fourth layers and 2.52% between the third and fourth layers. However, the difference decreases significantly after the 4th layer; for example, the %AAD of the 4th and 5th layers decreases to 1.25%, which is almost the same. An analysis of the density distributions of layers 3, 4 and 5 in Fig. 16 reveals that the density values under each pressure are very close. In summary, compared with the number of molecular layers in pore walls with more than four layers, the adsorption capacity and density values under the fourth layer basically reach a maximum, which reflects the adsorption capacity of the entire pore.

The number of solid molecular layers still affects the adsorption capacity and density value to a certain extent after the fourth layer. However, pursuing an excessive number of molecular layers is impractical because of the need to balance computational efficiency and accuracy. Our objective is to maintain high accuracy while minimizing computational intensity. Specifically, in computational methods such as MS and DFT, increasing the number of solid molecular layers significantly escalates computational demands (Steele and Bojan, 1998). Therefore, four layers of pore walls are deemed sufficient for accurate adsorption calculations.

4.5. Influence of different fluid-fluid interactions on the adsorption of the spherical SLD model

As outlined in Section 2, for the development of the spherical SLD model, the parameters b_{ads} and b represent the repulsive forces of the adsorbed phase and bulk phase, respectively. These parameters quantify the repulsive interactions between fluid molecules and indicate the volume occupied by fluid molecules within the pore adsorbed phase or bulk phase. The interaction between solid and fluid molecules at the pore results in a deviation in the volume occupied by the adsorbed phase near the pore wall compared with that in the bulk phase away from the pore wall. To accurately capture this deviation, we introduce an adjustable parameter Λ_b. This parameter not only characterizes variations in intermolecular repulsion across different regions but also significantly enhances the computational accuracy of the SLD model.

In general, when the SLD model is utilized for regression analysis of adsorption isotherms, accurate fitting of experimental data can be achieved primarily by adjusting the value of Λ_b. With the parameters $\varepsilon_{fs}/k_B = 4.85$ K and $R_s = 1.49$ nm fixed, we fit the laboratory excess adsorption isotherm at 353.15 K. As illustrated in Fig. 17, Λ_b generally tends to decrease with increasing pressure. A positive value of Λ_b indicates an increase in repulsive forces within the adsorbed phase. The decrease in Λ_b with increasing pressure suggests that the difference in repulsive forces between the adsorbed phase and the bulk phase gradually diminishes. This phenomenon occurs because during the initial stage of pore pressure increase, the density of the adsorbed phase increases more rapidly than that of the bulk phase does, leading to the largest repulsion force difference. However, as the adsorption amount reaches its peak, the growth rate of the adsorbed phase density slows relative to that of the bulk phase, resulting in a reduction in the repulsive force difference.

To further investigate the impact of Λ_b on gas adsorption behavior in spherical pores, a series of repulsive force parameters (Λ_b = 0, 0.125, 0.25, 0.5, and 0.75) were selected. The

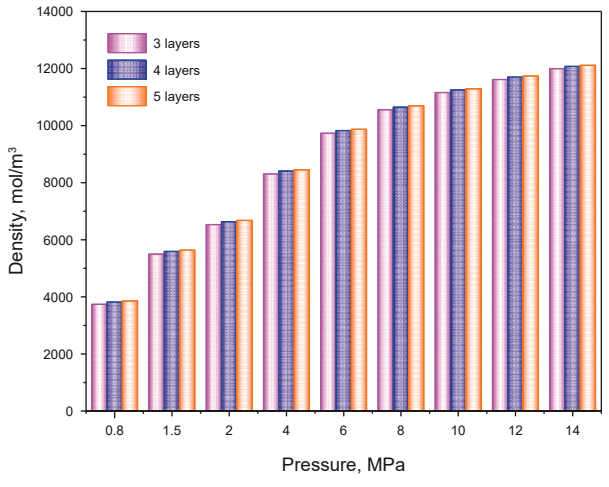

Fig. 16. Comparison of the density distributions under different solid molecular layers.

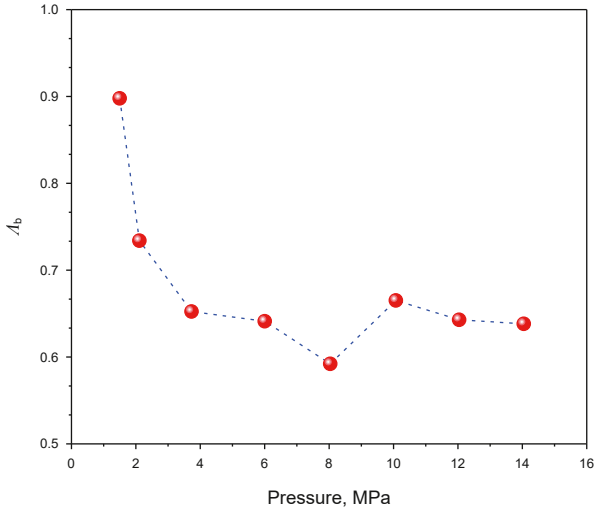

Fig. 17. The Λ_b used for fitting the laboratory adsorption isotherm at 353.15 K.

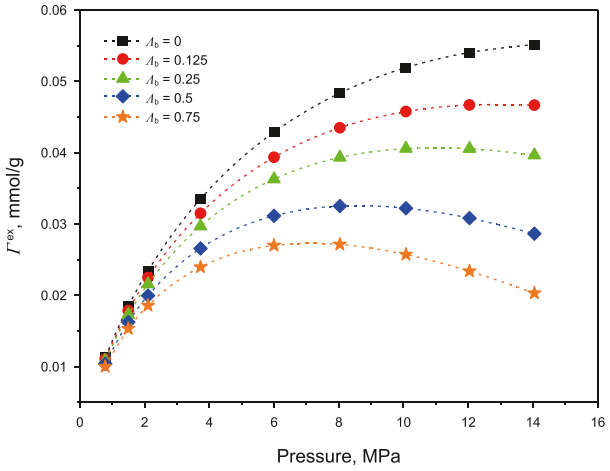

Fig. 18. Relationship between the excess adsorption isotherms and Λ_b at 353.15 K.

corresponding adsorption isotherms were calculated via the spherical SLD model, as illustrated in Fig. 18. As depicted in the figure, the excess adsorption capacity is negatively correlated with Λ_b; it decreases as Λ_b increases. Specifically, the higher the value of Λ_b is, the sooner the excess adsorption capacity reaches its peak. This phenomenon can be attributed to the fact that a larger Λ_b results in a stronger repulsive force within the adsorbed phase, leading to a reduced occupied space volume and consequently fewer gas molecules being adsorbed per unit volume. Therefore, the excess adsorption capacity continues to decrease. Additionally, the gas in the pores reaches saturation more readily at higher values of Λ_b.

5. Conclusions

On the basis of SLD theory, this paper proposes a new adsorption model that considers spherical pores for the first time. This model, by introducing a more accurate Peng-Robinson equation of state and a Lennard-Jones 10−4 potential function based on the spherical surface integral, can rapidly calculate the adsorption isotherms and density distributions within the spherical nanopores of shale. Compared with conventional theory models and traditional SLD models, the new model not only overcomes their shortcomings in characterizing the adsorption behavior within the complex pore structure of shale but also significantly improves the calculation accuracy of adsorption simulations, even with fewer fitting parameters. Through the verification and analysis of the new model, we draw the following conclusions regarding the methane adsorption mechanism within the spherical pores of shale:

(1) When the pore size and volume are the same, the maximum excess adsorption capacity of methane in spherical pores is 4.81 times greater than that in slit pores, and the maximum excess adsorption capacity of methane in cylindrical pores is 2.24 times greater than that in slit pores. The relationship of the maximum adsorption phase density is as follows: spherical > cylindrical > slit. The excess adsorption capacity and density of pores are strongly affected by their geometry. Therefore, if the geometric shape of the pores is ignored when characterizing the methane adsorption behavior in shale, it will cause a large error.

(2) When the pore diameter remains constant, the excess adsorption amount in the spherical pores first increases but then decreases as the pressure increases. When the pore diameter changes, the maximum excess adsorption amount in spherical pores less than 8 nm in diameter increases with increasing pore diameter, whereas in spherical pores greater than 8 nm in diameter, the maximum excess adsorption amount decreases with increasing pore diameter. Moreover, at high pressure, the maximum excess adsorption amount in the spherical pores can gradually become negative.

(3) For the different fluid-solid interactions within spherical pores, we verified that the optimal condition is when the solid molecular layer on the pore wall is 4 layers. Under these conditions, both the adsorption amount and density values are basically at their maximum values, which can reflect the complete adsorption capacity of the spherical pores in shale. For the repulsive force index Λ_b, which reflects the fluid-fluid interaction, we find that Λ_b has a negative correlation with the excess adsorption amount and pressure.

CRediT authorship contribution statement

Yu Zhao: Writing – review & editing, Methodology, Investigation, Funding acquisition. **Da-Guo Quan:** Writing – original draft. **Chao-Lin Wang:** Methodology, Investigation, Conceptualization. **Kun-Peng Zhang:** Software, Conceptualization.

Funding

This research was supported by National Natural Science Foundation of China (Nos. 52364004, 52264006, 52164001), the Guizhou Provincial Science and Technology Foundation (No. GCC[2022]005-1), and the Guizhou Provincial Graduate Research Foundation (2024YJSKYJJ068).

Declaration of competing interest

The authors declare that they have no known competing financial interests or personal relationships that could have appeared to influence the work reported in this paper.

Appendix

The adsorbed phase attractive parameter $a_{ads}(z)$ is a position-dependent parameter, that is proportional to the total configurational energy $\Phi(z)$ of the two-body interactions between an arbitrarily selected gas molecule in the pore and all surrounding molecules (Pang et al., 2020; Brańka and Heyes, 2006).

$$\frac{a_{ads}(z)}{a} = \frac{\Phi(z)}{\Phi_{bulk}} \tag{A1}$$

$$\Phi_{bulk} = -\frac{4\pi\varepsilon_{ff}\sigma_{ff}^3 N_A \rho_{bulk}}{3} \tag{A2}$$

To determine the configurational energy of gas molecules within spherical pores, a cylindrical coordinate system is established. An arbitrarily selected central molecule A serves as the origin, whereas molecule B represents any other molecule in the system. The virtual variable y denotes the axial distance in the cylindrical coordinate system, with $y = 0$ corresponding to the position where the center of molecule A is at a distance z from the inner wall of the pore. The angle θ represents the angular coordinate, and r signifies the radial distance within this coordinate system, as illustrated in Fig. A1.

The projected lengths of molecules A and B along the y-axis are easy to find. Therefore, to obtain the projected length of two molecules in the direction of the r-axis, we assumed that cross-section M-N passed through the center of molecule A and extracted cross-section M-N from the sphere pore for analysis, as shown in Fig. A2. When the distance between two molecules is the largest, the maximum projected length of the two molecules in the direction of the r-axis is $\sqrt{\left(R_s - 3\sigma_{ff}/8\right)^2 - (R_s - z - y)^2}$, as shown in Fig. A2(a). When two molecules are in contact with each other, the minimum projected length of the two molecules in the r-axis direction is $\sqrt{{\sigma_{ff}}^2 - y^2}$, as shown in Fig. A2(b). In addition, the arbitrary projected length of the two molecules on the cross-section M-N is $\sqrt{\left(R_s - 3\sigma_{ff}/8\right)^2 - (R_s - z - y)^2}/\cos\theta$, as shown in Fig. A2(c).

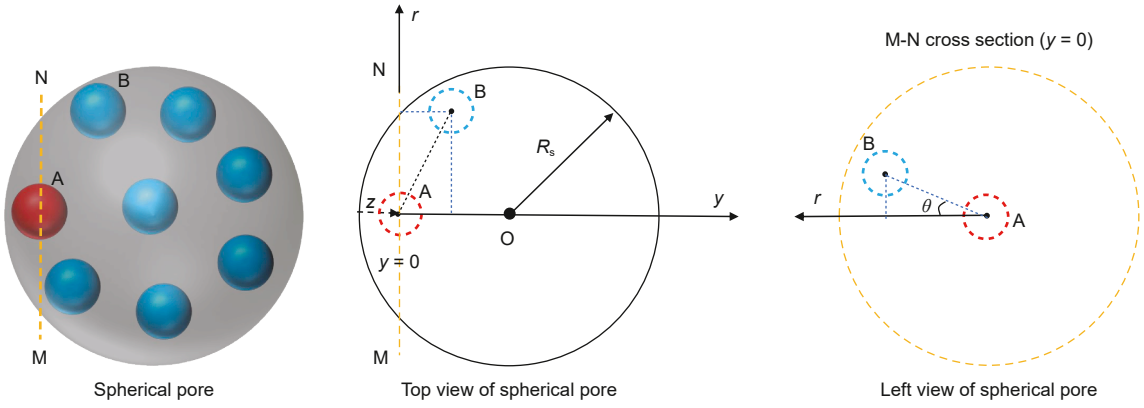

Fig. A1. Spherical porous cylindrical coordinate system.

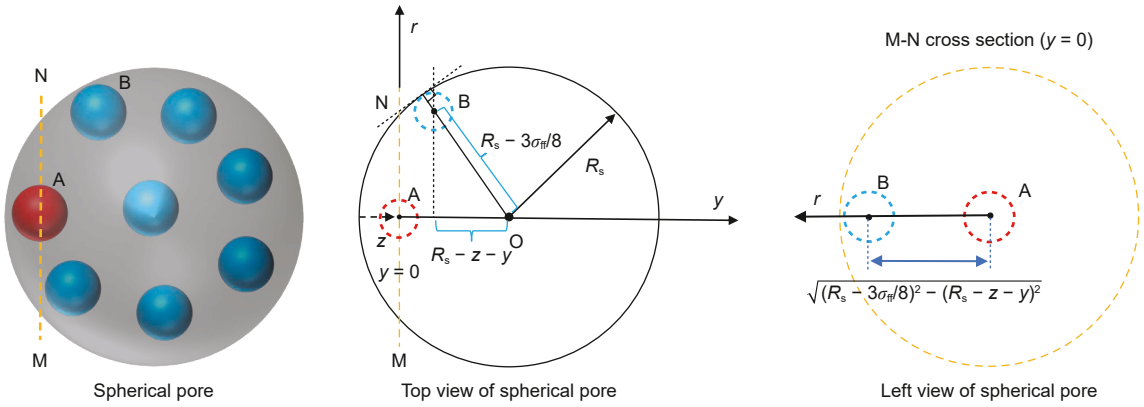

(a) Maximum projected length along the *r* axis on the M-N section of two molecules

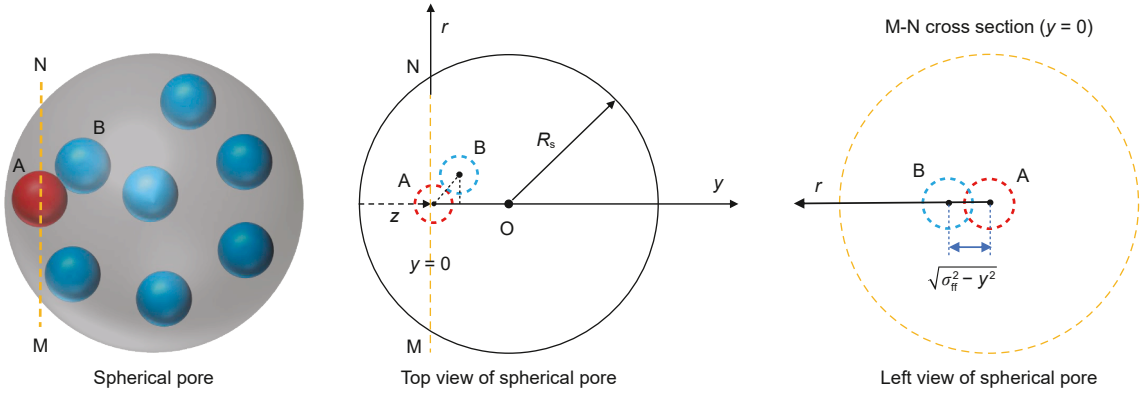

(b) Minimum projected length along the *r* axis on the M-N section of two molecules

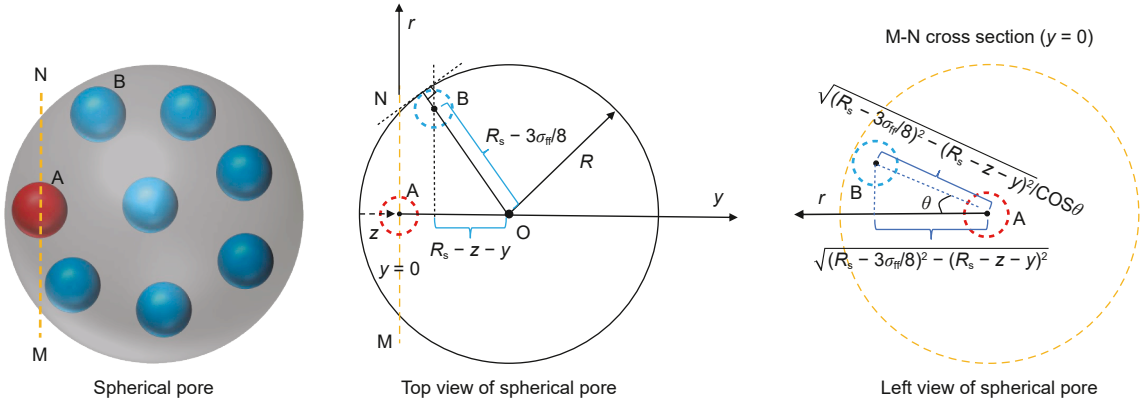

(c) Arbitrary projection length on the cross section of two molecules of M-N

Fig. A2. The projected length of two molecules on the cross-section M-N.

To summarize, we establish the geometric relationships among y, r, θ and z within the cylindrical coordinate system. Moreover, to refine the calculation of the configurational energy, the molecular configurational energy in spherical pores can be categorized into two primary scenarios on the basis of the ratio of the inner diameter D_s of the spherical pore to the diameter σ_{ff} of the gas molecules. Additionally, gas molecules within the pore are classified into two regions: those near the pore wall ($3\ \sigma_{ff}/8 \leq z < 11\ \sigma_{ff}/8$) and those distant from the pore wall ($11\ \sigma_{ff}/8 \leq z \leq R_s$).

Scenario 1: When $3 \leq D_s/\sigma_{ff}$, it can be divided into the following two calculation situations:

Situations 1.1: For $3\ \sigma_{ff}/8 \leq z < 11\ \sigma_{ff}/8$, the integral is calculated in the following three regions:

In region 1.1.1: y ranges from $3\ \sigma_{ff}/8 - z$ to 0,

$$\Phi_{111} = -4N_A\varepsilon_{ff}\sigma_{ff}^6\rho(z)\int_{3\sigma_{ff}/8-z}^{0}\int_{0}^{\frac{\pi}{2}} \times \int_{\sqrt{\sigma_{ff}^2-y^2}}^{\frac{\sqrt{\left(R_s-3\sigma_{ff}/8\right)^2-(R_s-y-z)^2}}{\cos\theta}} \frac{r}{\left(r^2+y^2\right)^3}\mathrm{d}r\mathrm{d}\theta\mathrm{d}y \quad (A3)$$

In region 1.1.2: y ranges from 0 to σ_{ff},

$$\Phi_{112} = -4N_A\varepsilon_{ff}\sigma_{ff}^6\rho(z)\int_0^{\sigma_{ff}}\int_0^{\frac{\pi}{2}} \times \int_{\sqrt{\sigma_{ff}^2-y^2}}^{\frac{\sqrt{(R_s-3\sigma_{ff}/8)^2-(R_s-y-z)^2}}{\cos\theta}} \frac{r}{(r^2+y^2)^3}\mathrm{d}r\mathrm{d}\theta\mathrm{d}y \quad (A4)$$

In region 1.1.3: y ranges from σ_{ff} to $D_s - 3\sigma_{ff}/8 - z$,

$$\Phi_{113} = -4N_A\varepsilon_{ff}\sigma_{ff}^6\rho(z)\int_{\sigma_{ff}}^{D_s-3\sigma_{ff}/8-z}\int_0^{\frac{\pi}{2}} \times \int_0^{\frac{\sqrt{(R_s-3\sigma_{ff}/8)^2-(R_s-y-z)^2}}{\cos\theta}} \frac{r}{(r^2+y^2)^3}\mathrm{d}r\mathrm{d}\theta\mathrm{d}y \quad (A5)$$

Therefore, for situation 1.1, the total configuration energy Φ_{11} is equal to the sum of the integrals of Φ_{111}, Φ_{112}, and Φ_{113}.

$$\Phi_{11} = \Phi_{111} + \Phi_{112} + \Phi_{113} \quad (A6)$$

Situations 1.2: For 11 $\sigma_{ff}/8 \le z \le R_s$, the integral is calculated in the following three regions:

In region 1.2.1: y ranges from 3 $\sigma_{ff}/8 - z$ to $-\sigma_{ff}$,

$$\Phi_{121} = -4N_A\varepsilon_{ff}\sigma_{ff}^2\rho(z)\int_{3\sigma_{ff}/8-z}^{-\sigma_{ff}}\int_0^{\frac{\pi}{2}} \times \int_0^{\frac{\sqrt{(R_s-3\sigma_{ff}/8)^2-(R_s-y-z)^2}}{\cos\theta}} \frac{r}{(r^2+y^2)^3}\mathrm{d}r\mathrm{d}\theta\mathrm{d}y \quad (A7)$$

In region 1.2.2: y ranges from $-\sigma_{ff}$ to σ_{ff},

$$\Phi_{122} = -4N_A\varepsilon_{ff}\sigma_{ff}^6\rho(z)\int_{-\sigma_{ff}}^{\sigma_{ff}}\int_0^{\frac{\pi}{2}} \times \int_{\sqrt{\sigma_{ff}^2-y^2}}^{\frac{\sqrt{(R_s-3\sigma_{ff}/8)^2-(R_s-y-z)^2}}{\cos\theta}} \frac{r}{(r^2+y^2)^3}\mathrm{d}r\mathrm{d}\theta\mathrm{d}y \quad (A8)$$

In region 1.2.3, y ranges from σ_{ff} to $D_s - 3\sigma_{ff}/8 - z$, and the integral calculation of the configuration energy Φ_{123} is the same as Eq. (A5).

Therefore, for situation 1.2, the total configuration energy Φ_{12} is equal to the sum of the integrals of Φ_{121}, Φ_{122}, and Φ_{123}.

$$\Phi_{12} = \Phi_{121} + \Phi_{122} + \Phi_{123} \quad (A9)$$

Scenario 2: When $2 \le D_s/\sigma_{ff} < 3$, it can be divided into the following two calculation situations:

Situations 2.1: For 3 $\sigma_{ff}/8 \le z < D_s - 11\ \sigma_{ff}/8$, the integral is calculated in the following three regions:

In region 2.1.1, y ranges from 3 $\sigma_{ff}/8 - z$ to 0, and the integral calculation of the configuration energy Φ_{211} is the same as Eq. (A3).

In region 2.1.2, y ranges from 0 to σ_{ff}, and the integral calculation of the configuration energy Φ_{212} is the same as Eq. (A4).

In region 2.1.3, y ranges from σ_{ff} to $D_s - 3\sigma_{ff}/8 - z$, and the integral calculation of the configuration energy Φ_{213} is the same as Eq. (A5).Therefore, for situation 2.1, the total configuration energy Φ_{21} is equal to the sum of the integrals of Φ_{211}, Φ_{212}, and Φ_{213}.

$$\Phi_{21} = \Phi_{211} + \Phi_{212} + \Phi_{213} \quad (A10)$$

Situations 2.2: For $D_s - 11\ \sigma_{ff}/8 \le z \le R_s$, the integral is calculated in the following two regions:

In region 2.2.1, y ranges from 3 $\sigma_{ff}/8 - z$ to 0, and the integral calculation of the configuration energy Φ_{221} is the same as Eq. (A3).

In region 2.2.2: y ranges from 0 to $D_s - 3\ \sigma_{ff}/8 - z$,

$$\Phi_{222} = -4N_A\varepsilon_{ff}\sigma_{ff}^6\rho(z)\int_0^{D_s-3\sigma_{ff}/8-z}\int_0^{\frac{\pi}{2}} \times \int_{\sqrt{\sigma_{ff}^2-y^2}}^{\frac{\sqrt{(R_s-3\sigma_{ff}/8)^2-(R_s-y-z)^2}}{\cos\theta}} \frac{r}{(r^2+y^2)^3}\mathrm{d}r\mathrm{d}\theta\mathrm{d}y \quad (A11)$$

Therefore, for situation 2.2, the total configuration energy Φ_{22} is equal to the sum of the integrals of Φ_{221} and Φ_{222}.

$$\Phi_{22} = \Phi_{221} + \Phi_{222} \quad (A12)$$

When $D_s/\sigma_{ff} < 2$, owing to the geometric constraints imposed by the spherical pore size, only a single gas molecule can be accommodated within the pore. Consequently, both the interaction energy parameter ε_{ff} and the overall configurational energy Φ are zero. Therefore, gas adsorption in spherical pores with diameters D_s less than twice the molecular diameter σ_{ff} is excluded from the statistical analysis.

References

Afsharpoor, A., Javadpour, F., 2016. Liquid slip flow in a network of shale noncircular nanopores. Fuel 180, 580–590. https://doi.org/10.1016/j.fuel.2016.04.078.

Amankwah, K.A.G., Schwarz, J.A., 1995. A modified approach for estimating pseudo-vapor pressures in the application of the Dubinin-Astakhov equation. Carbon 33 (9), 1313–1319. https://doi.org/10.1016/0008-6223(95)00079-S.

Appel, J., 1973. Freundlich's adsorption isotherm. Surf. Sci. 39 (1), 237–244. https://doi.org/10.1016/0039-6028(73)90105-2.

Baksh, M.S.A., Yang, R.T., 1991. Model for spherical cavity radii and potential functions of sorbates in zeolites. AIChE J. 37 (6), 923–930. https://doi.org/10.1002/aic.690370615.

Barrera, D., Dávila, M., Cornette, V., et al., 2013. Pore size distribution of ordered nanostructured carbon CMK-3 by means of experimental techniques and Monte Carlo simulations. Micropor. Mesopor. Mat. 180, 71–78. https://doi.org/10.1016/j.micromeso.2013.06.028.

Bernard, S., Horsfield, B., Schulz, H.M., et al., 2010. Multi-scale detection of organic and inorganic signatures provides insights into gas shale properties and evolution. Geochemistry 70, 119–133. https://doi.org/10.1016/j.chemer.2010.05.005.

Bi, H., Jiang, Z., Li, J., et al., 2016. The Ono–Kondo model and an experimental study on supercritical adsorption of shale gas: a case study on Longmaxi shale in southeastern Chongqing, China. J. Nat. Ggs. Sci. Eng. 35, 114–121. https://doi.org/10.1016/j.jngse.2016.08.047.

Brańka, A.C., Heyes, D.M., 2006. Thermodynamic properties of inverse power fluids. Phys. Rev. E 74 (3), 031202. https://doi.org/10.1103/PhysRevE.74.031202.

Brunauer, S., Deming, L.S., Deming, W.E., et al., 1940. On a theory of the van der Waals adsorption of gases. J. Am. Chem. Soc. 62 (7), 1723–1732. https://doi.org/10.1021/ja01864a025.

Brunauer, S., Emmett, P.H., Teller, E., 1938. Adsorption of gases in multimolecular layers. J. Am. Chem. Soc. 60 (2), 309–319. https://doi.org/10.1021/ja01269a023.

Cao, G.H., Lin, M., Ji, L.L., et al., 2019. Characterization of pore structures and gas transport characteristics of Longmaxi shale. Fuel 258, 116146. https://doi.org/10.1016/j.fuel.2019.116146.

Chabab, S., Coquelet, C., Rivollet, F., 2024. Generalization of the Wong-Sandler mixing rule to a generic cubic equation of state: examples of use for systems of industrial interest (hydrogen, CCUS, refrigeration). J. Supercrit. Fluids 212, 106336. https://doi.org/10.1016/j.supflu.2024.106336.

Chalmers, G.R.L., Bustin, R.M., 2008. Lower Cretaceous gas shales in northeastern British Columbia, Part II: evaluation of regional potential gas resources. Bull. Can. Pet. Geol. 56 (1), 22–61. https://doi.org/10.2113/gscpgbull.56.1.22.

Chen, J.H., Wong, D.S.H., Tan, C.S., et al., 1997. Adsorption and desorption of carbon dioxide onto and from activated carbon at high pressures. Ind. Eng. Chem. Res. 36, 2808–2815. https://doi.org/10.1021/ie960227w.

Chen, M.J., Kang, Y.L., Zhang, T.S., et al., 2018. Methane adsorption behavior on shale matrix at in-situ pressure and temperature conditions: Measurement and modeling. Fuel 228, 39–49. https://doi.org/10.1016/j.fuel.2018.04.145.

Curtis, J.B., 2002. Fractured shale-gas systems. AAPG Bull. 86 (11), 1921–1938. https://doi.org/10.1306/61EEDDBE-173E-11D7-8645000102C1865D.

Dubinin, M.M., 1967. Adsorption in micropores. J. Colloid Interf. Sci. 23 (4), 487–499. https://doi.org/10.1016/0021-9797(67)90195-6.

Dubinin, M.M., Astakhov, V.A., 1971. Development of the concepts of volume filling of micropores in the adsorption of gases and vapors by microporous adsorbents. Bulletin of the Academy of Sciences of the USSR. Div. Chem. Sci. 20 (1), 3–7. https://doi.org/10.1007/BF00849307.

Edwards, R.W.J., Celia, M.A., Bandilla, K.W., et al., 2015. A model to estimate carbon dioxide injectivity and storage capacity for geological sequestration in shale gas wells. Environ. Sci. Technol. 49 (15), 9222–9229. https://doi.org/10.1021/acs.est.5b01982.

Fitzgerald, J.E., Sudibandriyo, M., Pan, Z., et al., 2003. Modeling the adsorption of pure gases on coals with the SLD model. Carbon 41 (12), 2203–2216. https://doi.org/10.1016/S0008-6223(03)00202-1.

Fitzgerald, J.E., Robinson, R.L., Gasem, K.A.M., 2006. Modeling high-pressure adsorption of gas mixtures on activated carbon and coal using a simplified local-density model. Langmuir 22 (23), 9610–9618. https://doi.org/10.1021/la060898r.

Fu, H., Wang, X., Zhang, L., et al., 2015. Investigation of the factors that control the development of pore structure in lacustrine shale: A case study of block X in the Ordos Basin, China. J. Nat. Gas Sci. Eng. 26, 1422–1432. https://doi.org/10.1016/j.jngse.2015.07.025.

Gao, Z.Y., Liang, Z., Hu, Q.H., et al., 2021. A new and integrated imaging and compositional method to investigate the contributions of organic matter and inorganic minerals to the pore spaces of lacustrine shale in China. Mar. Petrol. Geol. 127, 104962. https://doi.org/10.1016/j.marpetgeo.2021.104962.

Gasem, K.A.M., Gao, W., Pan, Z., et al., 2001. A modified temperature dependence for the Peng–Robinson equation of state. Fluid Phase Equilibr 181 (1), 113–125. https://doi.org/10.1016/S0378-3812(01)00488-5.

Gasparik, M., Bertier, P., Gensterblum, Y., et al., 2014a. Geological controls on the methane storage capacity in organic-rich shales. Int. J. Coal Geol. 123, 34–51. https://doi.org/10.1016/j.coal.2013.06.010.

Gasparik, M., Rexer, T.F.T., Aplin, A.C., et al., 2014b. First international inter-laboratory comparison of high-pressure CH_4, CO_2 and C_2H_6 sorption isotherms on carbonaceous shales. Int. J. Coal Geol. 132, 131–146. https://doi.org/10.1016/j.coal.2014.07.010.

Gor, G.Y., Thommes, M., Cychosz, K.A., et al., 2012. Quenched solid density functional theory method for characterization of mesoporous carbons by nitrogen adsorption. Carbon 50 (4), 1583–1590. https://doi.org/10.1016/j.carbon.2011.11.037.

Guo, D., Zhang, L., Zhao, Y., et al., 2024. Impact of the water content on CO_2 and CH_4 adsorption and diffusion in quartz nanopores: A comprehensive study using GCMC, MD, and DFT. Colloid Surface A 703, 135442. https://doi.org/10.1016/j.colsurfa.2024.135442.

Hasanzadeh, M., Dehghani, M.R., Feyzi, F., et al., 2010. A new simplified local density model for adsorption of pure gases and binary mixtures. Int. J. Thermophys 31 (11), 2425–2439. https://doi.org/10.1007/s10765-010-0827-4.

Huang, C., Ju, Y., Zhu, H., et al., 2020. Investigation of formation and evolution of organic matter pores in marine shale by helium ion microscope: An example from the Lower Silurian Longmaxi Shale, South China. Mar. Petrol. Geol. 120, 104550. https://doi.org/10.1016/j.marpetgeo.2020.104550.

Huber, U., Stoeckli, F., Houriet, J.P., 1978. A generalization of the Dubinin-Radushkevich equation for the filling of heterogeneous micropore systems in strongly activated carbons. J. Colloid Interf. Sci. 67 (2), 195–203. https://doi.org/10.1016/0021-9797(78)90002-4.

Jakubov, T.S., Mainwaring, D.E., 2002. Modified Dubinin–Radushkevich/Dubinin–Astakhov adsorption equations. J. Colloid Interf. Sci. 252 (2), 263–268. https://doi.org/10.1006/jcis.2002.8498.

Kalkreuth, W., Holz, M., Levandowski, J., et al., 2013. The coalbed methane (CBM) potential and CO_2 storage capacity of the Santa Terezinha Coalfield, Paraná Basin, Brazil–3D modelling, and coal and carbonaceous shale characteristics and related desorption and adsorption capacities in samples from exploration borehole CBM001-ST-RS. Energ Explor. Exploit. 31 (4), 485–527. https://doi.org/10.1260/0144-5987.31.4.485.

Langmuir, I., 1918. The adsorption of gases on plane surfaces of glass, mica and platinum. J. Am. Chem. Soc. 40 (9), 1361–1403. https://doi.org/10.1021/ja02242a004.

Li, X., Chen, S., Wu, J., et al., 2023. Microscopic occurrence and movability mechanism of pore water in deep shale gas reservoirs: A typical case study of the Wufeng-Longmaxi Formation, Luzhou block, Sichuan Basin. Mar. Petrol. Geol. 151, 106205. https://doi.org/10.1016/j.marpetgeo.2023.106205.

Li, Z., Ren, T., Li, X., et al., 2023. Multi-scale pore fractal characteristics of differently ranked coal and its impact on gas adsorption. Int. J. Min. Sci. Technol. 33 (4), 389–401. https://doi.org/10.1016/j.ijmst.2022.12.006.

Liu, K.Q., Zakharova, N., Adeyilola, A., et al., 2021. Experimental study on the pore shape damage of shale samples during the crushing process. Energy Fuels 35 (3), 2183–2191. https://doi.org/10.1021/acs.energyfuels.0c03297.

Liu, R., Hao, F., Engelder, T., et al., 2020. Influence of tectonic exhumation on porosity of Wufeng–Longmaxi shale in the Fuling gas field of the eastern Sichuan Basin, China. AAPG Bull 104 (4), 939–959. https://doi.org/10.1306/08161918071.

Liu, Y., Wang, W., Wang, A., 2012. Effect of dry grinding on the microstructure of palygorskite and adsorption efficiency for methylene blue. Powder Technol. 225, 124–129. https://doi.org/10.1016/j.powtec.2012.03.049.

Löhr, S.C., Baruch, E.T., Hall, P.A., et al., 2015. Is organic pore development in gas shales influenced by the primary porosity and structure of thermally immature organic matter? Org. Geochem. 87, 119–132. https://doi.org/10.1016/j.orggeochem.2015.07.010.

Montgomery, S.L., Jarvie, D.M., Bowker, K.A., et al., 2005. Mississippian Barnett Shale, Fort Worth basin, north-central Texas: Gas-shale play with multi–trillion cubic foot potential. AAPG Bull. 89 (2), 155–175. https://doi.org/10.1306/09170404042.

Myers, A.L., Monson, P.A., 2002. Adsorption in porous materials at high pressure: theory and experiment. Langmuir 18 (26), 10261–10273. https://doi.org/10.1021/la026399h.

Ono, S., Kondo, S., 1960. Molecular Theory of Surface Tension in Liquids. Springer Berlin Heidelberg, pp. pp134–pp280. https://doi.org/10.1007/978-3-642-45947-4_2.

Pang, W., Jin, Z., 2019. Revisiting methane absolute adsorption in organic nanopores from molecular simulation and Ono-Kondo lattice model. Fuel 235, 339–349. https://doi.org/10.1016/j.fuel.2018.07.098.

Pang, Y., Hu, X., Wang, S., et al., 2020. Characterization of adsorption isotherm and density profile in cylindrical nanopores: Modeling and measurement. Chem. Eng. J. 396, 125212. https://doi.org/10.1016/j.cej.2020.125212.

Pfeifer, P., Obert, M., Cole, M.W., et al., 1997. Fractal bet and FHH theories of adsorption: A comparative study. Proc. Roy. Soc. Lond. Math. Phys. Sci. 423 (1864), 169–188. https://doi.org/10.1098/rspa.1989.0049.

Qajar, A., Daigle, H., Prodanović, M., 2016. The effects of pore geometry on adsorption equilibrium in shale formations and coal-beds: Lattice density functional theory study. Fuel 163, 205–213. https://doi.org/10.1016/j.fuel.2015.09.061.

Rangarajan, B.K., Lira, C.T., Subramanian, R., 1995. Simplified local density model for adsorption over large pressure ranges. AIChE J. 41, 838–845. https://doi.org/10.1002/aic.690410411.

Ravikovitch, P.I., Neimark, A.V., 2002. Density functional theory of adsorption in spherical cavities and pore size characterization of templated nanoporous silicas with cubic and three-dimensional hexagonal structures. Langmuir 18 (5), 1550–1560. https://doi.org/10.1021/la0107594.

Ross, D.J.K., Bustin, R.M., 2008. Characterizing the shale gas resource potential of Devonian–Mississippian strata in the Western Canada sedimentary basin: Application of an integrated formation evaluation. AAPG Bull 92 (1), 87–125. https://doi.org/10.1306/09040707048.

Sakurovs, R., Day, S., Weir, S., et al., 2007. Application of a modified Dubinin−Radushkevich equation to adsorption of gases by coals under supercritical conditions. Energy Fuels 21 (2), 992–997. https://doi.org/10.1021/ef0600614.

Santos, J.M., Akkutlu, I.Y., 2013. Laboratory measurement of sorption isotherm under confining stress with pore-volume effects. SPE J. 18, 924–931. https://doi.org/10.2118/162595-PA.

Siderius, D.W., Gelb, L.D., 2011. Extension of the Steele 10-4-3 potential for adsorption calculations in cylindrical, spherical, and other pore geometries. J. Chem. Phys. 135 (8), 084703. https://doi.org/10.1063/1.3626804.

Song, W., Yao, J., Ma, J., et al., 2018. Grand canonical Monte Carlo simulations of pore structure influence on methane adsorption in micro-porous carbons with applications to coal and shale systems. Fuel 215, 196–203. https://doi.org/10.1016/j.fuel.2017.11.016.

Steele, W.A., Bojan, M.J., 1998. Simulation studies of sorption in model cylindrical micropores. Adv. Colloid Interfac. 76-77, 153–178. https://doi.org/10.1016/S0001-8686(98)00045-1.

Sudibandriyo, M., Pan, Z., Fitzgerald, J.E., et al., 2003. Adsorption of methane, nitrogen, carbon dioxide, and their binary mixtures on dry activated carbon at 318.2 K and pressures up to 13.6 MPa. Langmuir 19 (13), 5323–5331. https://doi.org/10.1021/la020976k.

Sun, C., Nie, H., Dang, W., et al., 2021. Shale gas exploration and development in China: Current status, geological challenges, and future directions. Energy Fuels 35 (8), 6359–6379. https://doi.org/10.1021/acs.energyfuels.0c04131.

Sun, W., Zuo, Y., Wu, Z., et al., 2020. Pore characteristics and evolution mechanism of shale in a complex tectonic area: Case study of the Lower Cambrian Niutitang Formation in Northern Guizhou, Southwest China. J. Petrol. Sci. Eng. 193, 107373. https://doi.org/10.1016/j.petrol.2020.107373.

Swenson, H., Stadie, N.P., 2019. Langmuir's theory of adsorption: A centennial review. Langmuir 35 (16), 5409–5426. https://doi.org/10.1021/acs.langmuir.9b00154.

Tang, C.A., Webb, A.A.G., Moore, W.B., Wang, Y.Y., Ma, T.H., Chen, T.T., 2020. Breaking Earth's shell into a global plate network. Nat. Commun. 11 (1), 3621.

Tinni, A., Sondergeld, C.H., Rai, C.S., 2017. Hydrocarbon storage mechanism in shale reservoirs and impact on hydrocarbon production. SPE/AAPG/SEG Unconventional Resources Technology Conference. https://doi.org/10.15530/urtec-2017-2697659.

Wang, C., Zhang, K., Zhao, Y., et al., 2022. An adsorption model for cylindrical pore and its method to calculate pore size distribution of coal by combining NMR. Chem. En.g J. 450, 138415. https://doi.org/10.1016/j.cej.2022.138415.

Wang, C., Zhao, Y., Wu, R., et al., 2024. Shale reservoir storage of hydrogen: Adsorption and diffusion on shale. Fuel 357, 129919. https://doi.org/10.1016/j.fuel.2023.129919.

Wang, J., Tan, X.F., Tian, J.C., et al., 2021. The effect of diagenetic evolution on shale gas exploration and development of the Longmaxi Formation Shale, Sichuan Basin, China. Front. Earth Sci. 9, 661581. https://doi.org/10.3389/feart.2021.661581.

Wang, S., Feng, Q.H., Javadpour, F., et al., 2019. Competitive adsorption of methane and ethane in montmorillonite nanopores of shale at supercritical conditions: A grand canonical Monte Carlo simulation study. Chem. Eng. J. 355, 76–90. https://doi.org/10.1016/j.cej.2018.08.067.

Wu, X., He, Y., Ning, Z., et al., 2022. Mechanistic insights into confined methane adsorption in carbon nanopores at the molecular level. Chem. Eng. Sci. 250, 117374. https://doi.org/10.1016/j.ces.2021.117374.
Wu, X.J., Ning, Z.F., Cheng, Z.L., et al., 2019. Simplified local density model for gas adsorption in cylindrical carbon pores. APPL Surf. Sci. 491, 335–349. https://doi.org/10.1016/j.apsusc.2019.05.350.
Xiong, F., Rother, G., Gong, Y., et al., 2021. Reexamining supercritical gas adsorption theories in nano-porous shales under geological conditions. Fuel 287, 119454. https://doi.org/10.1016/j.fuel.2020.119454.
Yang, Y.F., Liu, J., Yao, J., et al., 2020. Adsorption behaviors of shale oil in kerogen slit by molecular simulation. Chem. Eng. J. 387, 124054. https://doi.org/10.1016/j.cej.2020.124054.
Yao, Y., Liu, D., Tang, D., et al., 2008. Fractal characterization of adsorption-pores of coals from North China: an investigation on CH_4 adsorption capacity of coals. Int. J. Coal Geol. 73 (1), 27–42. https://doi.org/10.1016/j.coal.2007.07.003.
Yin, N., Hu, Q.H., Liu, H.M., et al., 2022. Pore structure and wettability of lacustrine shale with carbonate interlayers in Dongying Depression, Bohai Bay Basin, East China. Front. Earth Sci. 10, 834640. https://doi.org/10.3389/feart.2022.834640.
Zaitseva, E.S., Tovbin, Y.K., 2023. Internal pressures of adsorbate in mesopores of different geometries and issues of analyzing the mechanisms of its flow. Prot. Met. Phys. Chem+ 59 (6), 1063–1072. https://doi.org/10.1134/s207020512370123x.
Zeng, Q., Wang, Z., McPherson, B.J., et al., 2017. Theoretical approach to model gas adsorption/desorption and the induced coal deformation and permeability change. Energy Fuels 31 (8), 7982–7994. https://doi.org/10.1021/acs.energyfuels.7b01105.
Zeng, Q., Wang, Z., McPherson, B.J., et al., 2017b. Modeling competitive adsorption between methane and water on coals. Energy Fuels 31 (10), 10775–10786. https://doi.org/10.1021/acs.energyfuels.7b01931.
Zeng, Q., Wang, Z., Sui, T., et al., 2021. Adsorption mechanisms of high-pressure methane and carbon dioxide on coals. Energy Fuels 35 (16), 13011–13021. https://doi.org/10.1021/acs.energyfuels.1c01094.
Zeng, X., Li, B., Gao, Z., et al., 2024. Studies into confined methane adsorption in shale nanopores using a simplified local density model. Chem. Eng. J. 488, 150985. https://doi.org/10.1016/j.cej.2024.150985.
Zhao, J.P., Chen, H., Zhang, J.Y., et al., 2022. Quantitative characterization of organic and inorganic pores in shale based on FIB-SEM. Front. Earth Sci. 10, 994312. https://doi.org/10.3389/feart.2022.994312.
Zhou, S., Zhang, D., Wang, H., et al., 2019. A modified BET equation to investigate supercritical methane adsorption mechanisms in shale. Mar. Petrol. Geol. 105, 284–292. https://doi.org/10.1016/j.marpetgeo.2019.04.036.